HAL
open science

Multifractal and multiscale entropy scaling of in-situ soil moisture time series: Study of SMOSMANIA network data, southwestern France

Sébastien Verrier

▶ **To cite this version:**

HAL Id: hal-02902866
https://hal.inrae.fr/hal-02902866

Submitted on 20 May 2022

1 **Multifractal and Multiscale Entropy scaling of in-situ soil moisture**

2 **time series: study of SMOSMANIA network data, southwestern**

3 **France**

4

5 Sébastien Verrier*

6 *Affiliation : (1) CESBIO, Université de Toulouse, CNES, CNRS, INRA, IRD, UPS, Toulouse, France.

7 (2) IUT Paul Sabatier, Auch, France

8 Correspondance : Dr. Sébastien Verrier, sebastien.verrier@iut-tlse3.fr

9

10

1 Introduction

12 Soil moisture is a key variable in hydrology, meteorology and biosphere science. It is the result of a

13 strongly heterogeneous atmospheric forcing, i.e. rainfall, and of the interaction of other processes

14 like evaporation, transpiration, or infiltration. Consequently, soil moisture is subject to strong and

15 possibly quick variations and is heterogeneous in space and time. This results in potential difficulties

16 in sampling strategies since sensors have their own limitations in terms of observable scales

17 (Vereecken et al., 2014). For instance, operating passive L-band radiometers like those of SMOS (Kerr

18 et al., 2010; 2016) and SMAP (Entekhabi et al., 2010) missions can provide continental daily coverage

19 of soil moisture variability but their spatial resolution is limited to pixels of about 50x50 km².

20 Airborne missions can provide more details about spatial variability but data are available over

21 limited areas and a very limited amount of time (i.e. when the mission is operated). Conversely, in-

22 situ sensors have the ability to give a very local estimate of soil moisture over small (hourly or sub-

23 hourly) time steps but their observations are difficult to upscale or to extrapolate to other locations.

24 This resolution mismatch may be somewhat reduced by applying downscaling methods to satellite

25 data (e.g., Merlin et al., 2008; 2011), but the problem is still not fully solved since downscaled

26 products have still coarse (kilometric) resolutions in comparison to the small spatial domain seen by

27 an in-situ sensor.

28 An alternative approach is to try to characterize the spatial and temporal variability of soil moisture

29 with intrinsically multiscale statistical formalisms. The idea behind such formalisms relies on the fact

30 that a complex, heterogeneous signal or random process may hide remarkable symmetries. In this

31 context, we may look for statistical estimators that could be related to the process resolution by

32 simple analytical laws. Such scaling properties are accurately followed by various geophysical

33 variables (Lovejoy, Schertzer et al., 2008; Lovejoy and Schertzer, 2006, 2010; Gagnon et al., 2006;

34 Tessier et al., 1993). In many cases, these properties are even related to the concepts of scale

35 invariance and fractality (some of these concepts will be defined in Section 2).

36 In geophysics, the characterization of scaling laws may be useful for several kinds of applications such

37 as: (i) comparing the variability of measurements collected by sensors operating at different

38 resolutions, (ii) evaluating a numerical model (such as a General Circulation Model or a Land Surface

39 Model) that should be able to reproduce some scaling features of the observations (e.g., Lovejoy et

40 al., 2013; Verrier et al., 2014), (iii) constraining statistical downscaling methods (Gires et al., 2012) to

41 respect the observed scaling laws.

42 In the context of soil moisture, existing studies already evidenced the existence of fractal-like scaling

43 in space and in time. In particular, remote sensing data have been used by several authors in order to

44 investigate fractal properties across space scales. Kim and Barros (2002a, 2002b) analyzed airborne

45 soil moisture estimates from the Southern Great Plains 1997 experiment and proposed a

46 monofractal approach for downscaling soil moisture from 10 km to 1km resolution. Multifractal

47 variants of the latter approach have been proposed later by Mascaro et al. (Mascaro and Vivoni,

48 2010, 2012; Mascaro et al., 2010, 2011) based on (partly similar) airborne remote sensing data sets.

49 Several analyses have also been performed on satellite images. For instance, Lovejoy, Tarquis et al.

50 (2008) have shown that both MODIS radiances and surface soil moisture index exhibit scaling and

51 multifractal properties (based on a case study over central Spain).

52 In the time domain, Katul et al. (2007) also identified the existence of spectral scaling properties

53 based on relatively long-term in-situ acquisitions (8 years of hourly data) at one specific station. The

54 authors also proposed a physical approach to justify the existence of these properties, especially

55 taking into account the integrative nature of soil water content with respect to its meteorological

56 forcing.

57 In the following, scaling analysis tools are applied to surface soil moisture time series collected by a

58 network of probes, SMOSMANIA. Overall, the SMOSMANIA network consists of about 20 stations

59 located in South-Western and South-Eastern France. Capacitive measurements of hourly soil

60 moisture have been done continuously during several years at stations belonging to the Météo-

61 France operational observation network. This makes these measurements suitable for scaling

62 analyses due to the wide range of time scales covered by the data. Moreover, the network design is

63 based on a compromise between a large spatial coverage and a moderate distance between probes.

64 Finally, all probes are located at places with relatively normalized conditions (flat areas, fallow

65 vegetation, low or moderate altitude) since they are co-located with operational meteorological

66 stations operated by Météo-France (Calvet et al., 2007; Albergel et al., 2010).

67 In this paper, a scaling analysis of eight-year long SMOSMANIA time series is proposed, based on

68 spectral and multifractal analysis tools. The objective will be to try to identify whether scaling

69 properties are present and over which scale range. Scaling will also be investigated in terms of

70 complexity analysis by computing the multiscale entropy (MSE) of the different time series.

71 The rest of the paper is structured as follows. In Section 2, theoretical notions related to spectral

72 scaling, multifractal scaling, and MSE are recalled. Then the dataset is presented in Section 3.

73 Spectral analysis results are then presented in Section 4, followed by the multifractal analysis of the

74 dataset in Section 5. MSE analysis of the data is detailed in Section 6. Then, in the subsequent Section

75 7, the expected relationship between MSE and multifractal scaling parameters is investigated with

76 the help of numerical simulations and discussed. Finally, I conclude in Section 8.

77

2 Theoretical background

78

2.1 Spectral scaling

79

80 Scale invariance consists of a family of generic properties exhibited by many geophysical datasets

81 (time series, 2D/3D fields). The concept is closely related to the concept of fractality that has been

82 investigated and popularized by B. Mandelbrot (e.g., Mandelbrot, 1983). In the context of stochastic

83 modeling of geophysical processes, scaling may be typically detected by investigating the scale

84 dependence of some classical or less classical statistical indicators that often vary as a power-law of

85 the time (or spatial) resolution or lag. The exponents of such power-laws can therefore characterize a

86 physical process over given range of scales. For instance, the approaches proposed by Kolmogorov

87 (1941) for turbulence or by Hurst (1951) in hydrological science have led to a vast scientific literature.

88 Among various statistical tools that can be used to investigate scaling properties, spectral analysis

89 offers a relatively simple and convenient way to study the distribution of energy across a wide range

90 of temporal or spatial frequencies. In particular, power spectral densities have been used as a tool to

91 investigate the temporal scaling properties of various hydrologic variables such as rainfall (Fraedrich

92 and Larnder, 1993; Olsson, 1995 ; Verrier et al., 2011), river flows (Pandey et al., 1998) or soil

93 moisture (Katul et al., 2007).

94 In the spectral sense, a time series is scaling if its power spectral density $E(f)$ is proportional to a

95 power law of the form:

96
$$E(f) \sim f^{-\beta} \qquad \text{(Eq.1)}$$

97 where f is the frequency and $\sim$ denotes equality within the limits of slowly varying factors that do not

98 affect the main scaling behavior. (Eq. 1) is valid for frequencies f comprised between two limit

99 frequencies defining the limits of the scaling range in which the scaling properties have been found.

100 For some processes like rainfall, several distinct scaling ranges may be found in the series, with

101 possible meteorological interpretation (e.g., Fraedrich and Larnder, 1993). In the case of soil

102 moisture, Katul et al. (2007) used theoretical and empirical arguments to separate two ranges, one

103 with a steep spectrum (behaving like $1/f^2$ spectrum or steeper) at high frequencies (equivalent to

104 time scales from hours to about one hundred hours) and another one with a flatter spectrum at

105 lower frequencies (i.e. larger time scales).

106

107 **2.2 Multifractals and cascades**

108 Multifractality may be viewed as a generalization of classical scaling properties to systems that do

109 not exhibit a unique scaling law per scaling range but a whole set of scaling laws with specific

110 parameters that nonlinearly depend on the order of statistical moments used in analysis (Schertzer

111 et al., 2002). Physically, it is interesting to investigate different orders of statistical moments since

112 they are representative of various levels of intensities of the process (e.g. moderate intensities vs.

113 extreme intensities).

114 Let us denote $\lambda = T/\tau$ the resolution factor consisting of the ratio of the series time length T and a

115 given analysis time scale τ (comprised between the time lag between two measurements and T). In

116 the strict sense, a time series $\Phi(t)$ is said to be multifractal if its statistical moments of real positive

117 orders q follow power-laws of the resolution λ:

118
$$\langle \Phi_\lambda^q \rangle \sim \lambda^{K(q)} \qquad \text{(Eq.2)}$$

119 In the previous equation, Φ_λ represents a low-resolution version of the original times series, obtained

120 by direct aggregation over disjoint intervals of length $\tau = T/\lambda$. Other approaches could have been

121   used for defining aggregated products (moving averages, wavelets…) but these approaches will not

122   be considered in the following.

123

124   In theoretical terms, stochastic processes following (Eq. 2) may be built by iterative multiplicative

125   procedures called multiplicative cascades (Schertzer et al., 2002). These procedures consist in a

126   series of resolution refinements where a given coarse scale series is modulated by random

127   multiplicative factors at each step (i.e. at each resolution refinement). Resolution refinements can be

128   done by explicitly dividing coarse pixels in smaller subpixels, thus causing a discretization of the

129   scales. Alternatively this construction can be extended to consider a continuum of scales, leading to

130   continuous in scale multiplicative cascades (Schertzer and Lovejoy, 1997). For the latter, random

131   multiplicative factors between two arbitrary scales should follow a log-infinitely divisible distribution.

132   In the general case described by (Eq. 2), the scaling exponent $K(q)$ is a convex function of the

133   moment order q. However, the exact form of $K(q)$ is subject to additional constraints when taking

134   into account the continuity of the scale space and the related constraints such as the distribution of

135   random multiplicative factors described above. Based on these considerations, some authors

136   proposed cascade models where the function $K(q)$ can be expressed in closed form. In particular,

137   two-parameter models have been proposed by Schertzer and Lovejoy (1987) and by She and Levêque

138   (1994).

139   In the following, the parameterization of the $K(q)$ function will be investigated with the help of the

140   Universal Multifractal (UM) model proposed by Schertzer and Lovejoy (1987). The choice of this

141   model was motivated by several factors such as its mathematical pertinence (the model is one of the

142   natural attractors of the class of continuous in scale log-infinitely divisible cascades), its wide use in

143   geophysical literature, and its physically interpretable parameterization.

144   In this framework, the function $K(q)$ is parameterized as follows:

145 $$K(q) = \frac{C_1}{\alpha-1}(q^\alpha - q) \quad \text{(Eq. 3)}$$

146   C_1 is a dispersion parameter comprised in the interval [0,1] for time series. For instance $C_1 = 0$ would

147   correspond to a homogeneous time series. Mathematically, C_1 is the fractal co-dimension associated

148   to the set of points exceeding a specific threshold specifically related to the mean value of the field .

149   The parameter α is an index of multifractality and belongs to the [0, 2] interval ($\alpha = 0$ is the pure

150   monofractal case where $K(q)$ becomes linear while $\alpha = 2$ corresponds to log-normal cascades for

151   which scaling exponents $K(q)$ vary in a quadratic way with q).

152

153

2.3 Fractionally integrated cascades

By construction, multiplicative cascades are potentially appropriate for modeling time series whose power spectrum follows a scaling law with a scaling exponent $\beta < 1$. More precisely the scaling exponent should follow the relationship $\beta = 1 - K(2)$ where $K(2)$ is necessarily positive (see, e.g., Tessier et al., 1993, §3.b).

However, most geophysical variables are characterized by steeper power spectra ($\beta > 1$) in space and/or time domains. This is typically the case for variables closely related to turbulence (where β is generally close to 5/3 for both wind speed and passive scalars coherently with the predictions of Kolmogorov (1941), Obukhov (1949), and Corrsin (1951)), but also for many other variables, including topographic fields (Gagnon et al., 2006). Anticipating on Sect. 4, the subsequent analyses of SMOSMANIA soil moisture will show evidence of power spectra that are closer to $1/f^2$ behavior.

In the latter cases, multifractality can be investigated by testing the validity of (Eq. 2) for a derivative of the process, called the flux and denoted Φ. This derivative can be a fractional derivative of the original process. It is recalled that fractional derivative and integrations are useful notions of fractional calculus that extend classical definitions of derivatives and integrals to non integer orders (Loverro, 2004). These concepts are useful for modeling processes with various spectral scaling exponents, e.g. integrations can represent effects leading to steeper power spectra (Schertzer and Lovejoy, 1991, appendix B2; Gagnon et al., 2006). In the context of our study, the observable variable Y (e.g., soil moisture) is modeled as the fractional integration of order H of a multifractal flux Φ that follow Eq.2. Combined with UM cascades, this defines the Fractionally Integrated Flux (FIF) model (Schertzer and Lovejoy, 1987) which depends of the three parameters α, C_1, and H. When H is positive, its effect is that of a smoothing parameter. On the contrary, the case $H < 0$ corresponds to additional roughening effects. The case $H = 0$ corresponds to multiplicative cascades described in the previous paragraph (i.e. without any additional smoothing or roughening).

In practice, this parameter H may also be estimated by computing the first-order structure function $S(\Delta t)$ defined by the first-order absolute increments of the time series as a function of the time lag Δt:

$$S(\Delta t) \stackrel{\text{def}}{=} \langle |Y(t + \Delta t) - Y(t)| \rangle \quad \text{(Eq.4)}$$

182   In the case of a FIF model, $S(\Delta t)$ follows a scaling law similar to the one exhibited by fractional

183   Brownian motions processes:

184    $$S(\Delta t) \sim \Delta t^H \quad \text{(Eq. 5)}$$

185   where ~ again means equality within the limits of slowly varying factors. It should be mentioned that

186   the definitions above can be extended by using other definitions of fluctuations in time series. For

187   instance, Lovejoy and Schertzer (2012) have proposed a variant based on the replacement of

188   difference fluctuations used in Eq. 4 by Haar fluctuations. Interestingly, such variants may differ from

189   each other in terms of range of validity of H estimates. For instance, structure functions estimates

190   based on Eq. 4 will allow the retrieval of H only when $0 < H < 1$. The use of Haar fluctuations can lead

191   to correct estimates on a wider range of H values ($-1 < H < 1$). In the rest of the paper, analyses will

192   nevertheless be based on the more classical structure functions defined by (Eq. 4). This is not a

193   limitation here since H estimates will be found near the middle of the [0, 1] interval (see section 6.2).

194   The value of H directly affects the distribution of energy across scales: namely, a higher value of H

195   implies a steeper spectrum. For a FIF series, both values are related by $\beta = 1 - K(2) + 2H$ (Tessier et al.,

196   1993). Note that for a monofractal signal such as a fractional Brownian motion (characterized by a

197   unique scaling exponent H), a more or less similar relationship ($\beta = 1 + 2H$) still holds. The case of FIF

198   processes differs from the fBm case by the multifractal correction term $K(2)$.

199

200   2.4 Multiscale entropy

201   Other signatures of scale-invariance may be found by using analysis methods more closely related to

202   information theory. For instance, the notion of information dimension has been defined to

203   characterize the density of points in fractal geometric sets and strange attractors (e.g., Hentschel and

204   Procaccia, 1983; Farmer et al., 1983). Zhang (1991) suggested computing Shannon entropies of

205   coarse-grained time series as a prerequisite to define a complexity measure of a signal. A similar

206   approach has been proposed by Costa et al. (2002, 2003, 2005) in the context of the analysis of

207   biological signals. Their approach, called Multiscale Entropy (MSE) is based on the estimation of the

208   sample entropy (SampEn) (Richman and Moorman, 2000) applied on time series that are coarse-

209   grained at various time resolutions. The sample entropy provides an approximation of the entropy

210   information of any discrete time series $y[i]$ of length N by computing the conditional probability that

211   two similar sequences of m consecutive points will remain similar when considering extended

212   sequences of $m+1$ points.

213 If $u_m[i]$ denotes a sequence (vector) of m points starting at index i, i.e. $u_m[i] = \{y[i], \dots, y[i + m -

214 1]\}$, and d is a given distance between vectors (here taken as the maximal absolute distance between

215 their components), then we may define the probability of similarity between two different vectors

216 with respect to a threshold T:

217 $$A(m, T, N) = \Pr(d(u_m[i], u_m[j]) \leq T) \qquad (j \neq i) \qquad (\text{Eq.} 6)$$

218 Then the sample entropy may be computed by estimating the negative logarithm of the conditional

219 probability that two matching vectors of length m will still match while taking into account an

220 additional point within all vectors (Costa et al., 2005):

221 $$S_E(m, T, N) = -ln\left(\frac{A(m + 1, T, N)}{A(m, T, n)}\right) \qquad (\text{Eq.} 7)$$

222 Due to the negative logarithm, the sample entropy tends to increase when "unexpected" changes in

223 the series tend to occur, i.e. when they are less repetitive and contain more information. In the

224 following, the parameters m and T will be fixed to values close to those used in the literature, i.e.

225 m = 2 and T taken as 15% of the standard deviation of the time series y.

226 Within this context, the Multiscale Entropy is a procedure consisting at estimating the sample

227 entropy not only from given a data time series $Y[i]$ but also from coarse-grained time series $Y^{(\tau)}[i]$

228 that may be estimated by averaging Y over non-overlapping windows of length τ. This provides an

229 entropy estimate MSE(τ) that depends on the time resolution τ.

230 Recent results tend to prove that scale invariance has a specific signature on the Multiscale Entropy:

231 as recalled by Nogueira (2017), MSE(τ) should scale as a power-law with exponents closely related

232 with the spectral slope., i.e.

233 $$MSE(\tau) \sim \tau^{H'} \qquad (\text{Eq.} 8)$$

234 This has been verified empirically in the case of colored noise/fractional Brownian motion (fBm) time

235 series (Courtiol et al., 2016). Analytical arguments based on fBm theory have also been proposed by

236 Gao et al. (2015) to understand this relationship. These authors also confirmed their findings on

237 empirical studies of biological signals.

238 Nogueira (2017) compared the scaling laws of power spectra and MSE approach for both geophysical

239 data (near-surface wind) and synthetic data (based on monofractal fBm series). In the case of

240 monofractal fBm signals, the results were tending to confirm that the MSE scaling exponent H'

241 should be identical to the scaling exponent H determined by the first-order structure function. On

242   the contrary, the case of multifractal signals has not been explicitly analyzed. It may be noticed that

243   Nogueira's empirical results on turbulent (i.e., likely multifractal) wind processes suggest that a

244   scaling law if the form of Eq. 8 could still hold for multifractal signals.

245   In the following, both MSE tools and multifractal analysis tools will be applied to the same

246   SMOSMANIA surface soil moisture time series. This will provide two types of multiscale information

247   that could eventually be compared.

248

249

3 Data sets

SMOSMANIA consists of a network of about 20 measurement stations distributed across Southwestern and Southeastern France in grassland and agricultural areas (Calvet et al., 2007; Albergel et al., 2010, 2011). This network has been set up in relation with the much broader HyMeX campaign (http://www.hymex.org) which was mainly devoted to the monitoring and modeling of water cycle within the Mediterranean region. The SMOSMANIA probes are located at existing operational Météo-France weather stations (RADOME network). The average distance between two SMOSMANIA stations is of the order of 45 km (Albergel et al., 2010). These locations may be viewed at ISMN website at the following address: www.geo.tuwien.ac.at/insitu/data_viewer/ISMN.php. All stations are located at places with a fallow vegetation cover.

The SMOSMANIA network provides operational measurements of volumetric soil moisture and soil temperatures at various depths. Concerning the former, soil moisture is estimated on a hourly basis with the help of Thetaprobe sensors based on a capacitive technology. Measurements are available at four references depths ranging from 5 cm to 30 cm. All the time series may be downloaded for free at the International Soil Moisture Network (ISMN) page (http://ismn.geo.tuwien.ac.at/data-access/). For more information about ISMN, the reader is also referred to the presentation by Dorigo et al. (2011).

The present study is focused on time series located in Southwestern France, i.e. on time series of soil moisture collected at 12 places reported in Table 1. Since scaling-related analyses must generally rely on data that have a small number of missing data, time series presenting long missing periods of several dozens of days have been discarded. We therefore restricted the study to nine of the twelve initial series (discarded series are marked with a star in Table 1). All remaining missing data have been replaced by linear interpolation.

Several differences between locations should be noted. For instance, Urgons, Sabres, and Créon d'Armagnac are located closer to the Atlantic ocean and therefore are subject to a more oceanic climate. They also differ from most of the other stations by a different soil texture with a much larger sand proportion. Stations that are closer to the Mediterranean Sea (Narbonne, Lézignan-Corbières) typically have a silt loam texture. Finally, stations that are distant from both seas tend also to have the largest clay fraction (Condom, Peyrusse Grande, Lahas). We can notice that all stations (except Mouthoumet station) are located at low altitudes.

281 The present study is focused on the 2007-2014 period that covers most of the available time series

282 from ISMN. Thus, all soil moisture measurements comprised between 2007/01/07 6:00 and

283 2015/01/01 0:00 (local time) have been selected in order to cover approximately 8 years.

284 Measurements before 2007/01/07 were only available at a few stations and thus were discarded.

285 Since all sensors provide measurements on an hourly basis, all selected time series have about

286 70,000 data points which provides the possibility of investigating potential scaling properties over

287 four orders of magnitude in scale.

288 Finally, some data at the beginning of the data series have been removed in order to reduce all the

289 time series to 65536 measurements points each. All the retained series still cover the same dates,

290 ending on 2015/01/01 0:00. The purpose of this restriction is to work with 2^n length time series

291 (here n = 16) which is preferable for technical reasons. Indeed, multifractal analysis requires the

292 estimation of statistical moments at different aggregated resolutions and the use of a dyadic cascade

293 (i.e. 2^i resolutions with integer i) is very convenient for this. Moreover, FFT-based spectral analysis

294 techniques are also faster when applied to series with 2^n data points.

295

296

297 4 Spectral analysis of SMOSMANIA series

298 4.1 Surface soil moisture data (5 cm depth)

299 Spectral analysis has been carried out on the data set of soil moistures measured at 5 cm depth in

300 order to identify scaling properties and possible scaling ranges. Since scaling properties generally

301 take the form of a power-law spectrum, i.e. $E(f) \sim f^{-\beta}$, the results are presented in logarithmic

302 coordinates. In such a graph, scaling laws should indeed appear as linear. However, this

303 representation may have less desirable counterparts when analyzing long time series. In particular,

304 this usually results in a much denser sampling of frequencies near the high frequencies and often in a

305 less readable graphic representation. To avoid these problems, an average of the spectra over

306 equally spaced logarithmic bins (of length 0.02 here) was performed.

307 The power spectra of the nine selected series are shown on Figure 1. The figure is presented in

308 logarithmic coordinates. In order to make it more readable, the spectra are translated upwards from

309 one station to the next one. The spectrum of the Condom series is the only one that has not been

310 vertically translated. Time scale tick labels are displayed on the horizontal axis (i.e. high frequencies

311 are still on the right of the figure but the horizontal graduations specify the time scale equivalent to
312 this frequency, i.e. $\tau = 1/f$).

313

314 The main feature exhibited by the spectra on Figure 1 is the presence of scaling laws over a large
315 scale range covering a large range of scales. All spectra seem nevertheless slightly steeper at the high
316 frequencies than at low frequencies. A more oscillatory behavior at low frequencies (e.g. time scales
317 larger than several thousands of days) may be noticed. This feature is probably related to the coarser
318 sampling of frequencies when analyzing large scale structures over time series that is not much
319 longer than these structures.

320 It may also be noticed that all spectra appear roughly parallel to each other which suggests that all
321 spectra should have very similar scaling laws with exponents β that are not expected to vary much.
322 This may be checked by calculating these scaling exponents.

323 While the spectra look scaling over three orders of magnitude at first glance, several additional
324 factors must be taken into account to determine the scale range considered in the fits: (i) the low-
325 frequency part of the spectrum has a poorer sampling and is less robustly estimated, (ii) the
326 application of a segmentation algorithm (D'Errico, 2017) has been used to identify possible
327 transitions between ranges with different spectral exponents β, but failed to notice very significant
328 transitions, (iii) however, some spectral estimations (for instance at Lahas station) exhibit a very local
329 drop at time scales of the order of 1000-3000 h, (iv) the retained fit range must permit linear
330 regressions with a good coefficient of determination, for example $R^2 > 0.98$.

331 Taking these elements into account and also anticipating on Sect. 5 where a narrower scaling range
332 will be found, the estimation of scaling exponents has been limited to the range of scales 1000h – 1h.
333 The linear regressions are shown on Figure 1 and the scaling coefficients β are reported in Table 2
334 (for the nine soil moisture time series collected at depth 5 cm). It may be noticed that this choice
335 permits one to obtain a very good coefficient of determination for each of the nine spectra
336 presented. All spectral slopes β are found within or very close to the range [1.9, 2] and thus are very
337 similar to each other when considering that each exponent is given with an uncertainty of ±0.04. This
338 confirms the apparent parallelism of the spectra on the figure.

339 **4.2 Other depths**

340 By repeating the above procedure for the three other depths, similar results were obtained with
341 scaling holding to a good approximation for scales smaller than 1000 h (all error bars $\Delta\beta$ were found

12

342 smaller than 0.04 for a linear fit within this range). For all time series, the surface (5 cm) data

343 spectrum remains above the other spectra, meaning that the surface series contains more energy (in

344 the signal processing sense) than the other ones. Physically, this is also coherent with the greater

345 variability amplitude of soil moisture at the surface due to the meteorological forcing.

346 However, significant differences have been found between stations with typical cases illustrated on

347 Figures 2a and 2b. At Peyrusse Grande station (Fig. 2a), the spectra are close to each other and the

348 spectral slopes do not change considerably with depth (here from 1.93 to 2.08) while at Montaut the

349 spectra are clearly distinct with different spectral slopes (ranging from 1.97 to 2.35). It may be noted

350 that the spectra displayed on Figure 2 do not include any vertical shifts between spectra.

351 The spectral slopes β estimated for all stations at all considered depths are summarized on Figure 3.

352 The estimates of β are represented on the vertical axis while the stations names are distributed on

353 the abscissa axis (the stations have been sorted from the most western position to the most eastern

354 position). More precisely, the abscissa axis refers to the three first letters of the names of the

355 stations. Error bars are omitted but are of the order of ±0.03 or 0.04 for all estimates.

356 As illustrated on Figure 2 and Figure 3, it seems that the spectral slope tends to increase as we

357 consider deeper layers. However, β estimates become more variable across stations as the depth

358 increases. This could possibly be related to the differences in subsurface processes and soil texture,

359 the latter being heterogeneous across the stations.

360 While similar studies in the region of interest do not seem to be reported in the literature, several

361 published studies may help to put our findings in perspective. In the space domain, lower scaling

362 exponents are generally reported. For instance, Pelletier et al. (1997) found a value of β = 1.8, while a

363 value closer to 1.2 might be deduced from the findings presented by Kim and Barros (2002a), based

364 on remote sensing data. More recently, Neuhauser et al. (2018) reported a spectral exponent closer

365 to 1.0 at spatial scales > 40 km based on SMOS data.

366 In the time domain, higher estimates of β have been reported by Katul et al. (2007) based on

367 measurements of soil moisture in a more subtropical eastern US region (Durham, NC). These authors

368 considered an eight-year long time series of integrated (0-30 cm) soil moisture. They found a steep

369 scaling β = 2.75 in the scale range 90 h – 1h and a much flatter spectrum at larger scales.

370 Interestingly, they also proposed a simplified physical model to show that soil moisture time series

371 may behave as a time integration of precipitation time series at relatively small time scales (at least

372 in first approximation). Since power spectra of precipitation data are either flat or decrease in a

373 scaling way (i.e. f^{-a} where a > 0, cf. Fraedrich and Larnder, 1993), the expected spectrum of soil

374   moisture could be of the form f^{2-a}, which was verified in their case. The results obtained by Katul et

375   al. (2007) therefore suggest that it is not surprising that soil moisture has a steeper scaling in the

376   time domain than in the space domain, due to this time integration effect. However, in the present

377   study estimates of β are found closer to 2.0, i.e. a red-noise like scaling. In this sense, our results may

378   differ from those of Katul et al. (2007) since the model proposed by the latter authors does not seem

379   compatible in practice with values of β smaller than 2.

380

5 Multifractal analysis

381

5.1 Surface soil moisture data (5 cm depth)

382

383   Results of the previous section show that soil moisture power spectra estimated above are rather

384   steep (similar to a f^{-2} red-noise). This usually means that the series cannot be directly described by a

385   multifractal multiplicative cascade which requires β < 1. However, as explained in Section 2.3, it is

386   possible to check whether a multifractal cascade structure may describe some derivative (or

387   integration) of the process. Fractionally integrated stochastic processes (e.g. fractional Brownian

388   motions, fractionally integrated flux…) are models that may be appropriate for scaling processes with

389   steeper spectral slopes. Therefore, a possible way to investigate multifractality within the series is to

390   consider a "flux" estimated from a derivative of the time series and to test whether the moments of

391   this flux follow a multifractal law analogous to that described in Section 2.2 (Eq. 2).

392   In the following, the fluxes Φ are estimated at 1h resolution by taking the absolute value of the finite

393   difference derivative of the 5cm moisture series, following the process originally described by

394   Lavallée et al. (1991, 1993). For each series, the flux is aggregated over non-overlapping intervals of

395   length τ = $2^i \tau_0$ using a dyadic cascade approach (i.e. at each step the resolution ratio λ = T/τ is

396   divided by a factor two and the data are aggregated on successive couples of points). This leads to an

397   ensemble of aggregated fluxes series $\Phi_\lambda(t_i)$ indexed by the resolution $\lambda = 2^j$ for j = 0, 1, …, 16 (each

398   aggregated series thus containing λ data points).

399   Then the empirical moments are used as an estimate of the (unknown) statistical moments. For each

400   series, and for each chosen moment order q, the aggregated fluxes are elevated to power q and

401   averaged over the whole series length. The computation is done for all averaging resolutions $\lambda = 2^j$

402   (j = 0,1,…, 16) and for various orders q comprised between 0 and 2.5 (with a spacing of 0.1 between

403   two successive orders). This provides the empirical moments $M(\lambda, q)$ that approximate the statistical

404   moments $\langle \Phi_\lambda^q \rangle$, the statistical average being replaced by the empirical average. This procedure

405   corresponds to the Trace Moment approach presented by Tessier et al. (1993).

406   The empirical moments are represented in logarithmic coordinates as a function of the resolution λ.

407   The process is repeated for each series. The result is displayed in a larger figure for the case of

408   Peyrusse Grande data, and in a composite figure for other stations (see Figures 4 and 5).

409   Figure 4 may be read as follows. First, each curve is associated to one specific moment order. The

410   higher moment orders $q > 1$ are associated with the upper, increasing curves on the figure, while the

411   slightly decreasing curves are associated to orders q such that $0 < q < 1$. Similarly to Figure 1, finer

412   resolutions are located on the right of Figure 4.

413   At the coarsest time scales, typically > 1000 h, the curves are undistinguishable meaning that no

414   significant multiscaling may be found. However, moments are much more variable towards finer

415   resolutions. Log-log linear behavior is found to a good approximation within the range of resolutions

416   comprised between 128 h and 1 h (green fit lines). Since the figure is in logarithmic coordinates, each

417   regression is representative of Eq. 2 for a fixed order of moment q and its slope corresponds to the

418   scaling exponent $K(q)$.

419   Comparable figures are found for the eight others time series with very similar scaling ranges

420   (Figure 5). Thus, and in order to facilitate the comparison between the different series, it has been

421   chosen to perform the regression over the same scaling range (128 h – 1 h). It can be noted that this

422   range is smaller than the one observed on power spectra presented in the previous section.

423   Based on Figure 4, we also remark that all linear regressions are convergent towards a point while

424   being extrapolated towards coarser resolutions. The abscissa of this point may correspond to the

425   "external scale" (Lovejoy et al., 2008) at which the multifractal cascade is initiated. For the nine time

426   series, the exact position of the external scale may vary a bit but is comprised in the range 200-600

427   hours. For most of the time series, the external scale would be close to 200-300 h, but for some of

428   them higher values seem obtainable (e.g., Urgons, Narbonne, or Créon d'Armagnac). For the latter

429   station, the external scale seems indeed closer to 600 h. Due to the uncertainty of this estimate, it is

430   not possible to clearly tell if the latter difference is really significant and related to meteorological

431   forcing. Nevertheless, the position of the external scale is plausibly related to the

432   weather/macroweather transition scale that has been evidenced for numerous atmospheric fields

433   (Lovejoy et al., 2013; de Lima and Lovejoy, 2015). The transition between the weather and

434   macroweather regimes occurs at the lifetime of planetary meteorological structures, i.e. at time

435   scales of the order of a couple of weeks. For meteorological variables, the transition separates

436 scaling regime respectively characterized by a small intermittency (i.e. large-scale/macroweather)

437 and a stronger (multifractal) intermittency at smaller scales (i.e. weather regime).

438 As explained above, the slopes of the green lines on Figure 4 provide the estimates of the moment

439 scaling function $K(q)$ for the orders q that have been used in previous computations. The graph of the

440 estimated $K(q)$ function at Peyrusse Grande station is provided on Figure 6. The round dots

441 correspond to the empirical estimates. We may notice that the values of $K(q)$ are also given for

442 higher moment orders (up to 3.0) that have not been represented on Fig. 4 for readability purposes.

443 As expected, the $K(q)$ estimates are distributed along a convex curve. The latter may then be fitted by

444 the two-parameter universal form recalled in Section 3. The green curve is obtained by nonlinear

445 optimization on the interval defined by $q \in [0, 2.5]$. More precisely, the Nelder-Mead method is

446 used to find the couple of parameters that minimizes the (quadratic) distance between fixed $K(q)$

447 estimates and the theoretical values predicted by (Eq. 3). In this case, the universal parameters

448 estimates for Peyrusse Grande station are $C_1 = 0.28$ and $\alpha = 1.51$.

449 For other stations, more or less similar graphs may be obtained but some variability still exists in both

450 estimates of α and C_1 (Fig. 9). All the different $K(q)$ function estimates were fitted within the interval

451 $[0, 2.5]$ (see Figure 5). The obtained parameters are reported in Table 3.

452

453 As shown on Table 3, some variability may be found within parameter estimates. Nevertheless,

454 C_1 remains always close to 0.25-0.3 and the observed variability does not seem related with the

455 positions of the stations and/or soil texture. Such estimates are significantly larger than the values

456 (closer to 0.1 or even less) reported for other geophysical fields (e.g., Lovejoy and Schertzer, 2013).

457 However, some studies report large (> 0.3) estimates in the case of rainfall (e.g., Lovejoy, Schertzer et

458 al., 2008), at least at time scales larger than 1 h (Verrier et al., 2011). Thus, the relatively high value of

459 C_1 that has been observed in this study for soil moisture could be a consequence of the large

460 intermittency of the rainfall process. Concerning the index of multifractality α, most estimates are

461 found within the range 1.6-1.8. In this aspect, the stations of Créon d'Armagnac and Urgons seem to

462 differ significantly from the others with much lower α estimates closer to 1.3-1.4. Interestingly, these

463 stations are relatively close to each other (about 55 km) and both located in the French department

464 of Landes, at the most western part of the region covered by SMOSMANIA, i.e. closer to the Atlantic

465 Ocean and with significantly more sandy soil texture. This could suggest a possible impact of these

466 features on α. However, the parameter α characterizes the degree of nonlinearity of the $K(q)$ curve

467 and is known to be more difficult to estimate than C_1. This could also explain part of the observed

468 difference despite the relative homogeneity of α estimates for the other stations.

469

470 **5.2 Other depths**

471 By repeating the previous analysis to other depths, a similar multifractal scaling was found in the

472 range 128 h – 1 h for all stations. This is illustrated on Figure 8 where moments of Peyrusse Grande

473 (10, 20, 30 cm) data follow a scaling law that could be extrapolated to external scales of the order of

474 several hundreds of hours. From the slopes of the green lines, scaling exponents $K(q)$ may be

475 computed and then plotted on Figure 8 (bottom right). On this figure, each color is associated to one

476 depth (note that 5 cm depth estimates are also plotted on the same graph). While the different

477 curves globally follow the same shape, they differ significantly from each other for low and high

478 moment orders. In this case, high-order moments are higher for 10 cm depth data than for other

479 data, while 20 cm depth data differ from the others for low moment orders. These differences affect

480 both estimates of multifractal parameters, which can be checked by comparing the couples (α, C_1) at

481 depths 5 cm and 20 cm. Indeed, the latter are respectively equal to (1.51, 0.28) and (0.79, 0.40). Part

482 of the change may be explained by the partial "linearization" of the $K(q)$ curve as the depth increases

483 (the limit case of linearity can theoretically be attained at α = 0, i.e. monofractality case).

484 For all time series, the parameters α and C_1 have been estimated at the different depths. The results

485 are summarized on Figures 9a and 9b where estimates are given as a "function" of the station (once

486 again, stations are sorted from the most western to the most eastern and are identified by their first

487 three letters). As deeper data are considered, smaller values of α and larger values of C_1 are

488 systematically obtained, with a globally larger variability from one station to one another. Similar to

489 Fig. 8, this change seems to be related to a less pronounced convexity of the $K(q)$ curves as depth

490 increases.

491 We may conclude that soil moisture at these depths still follows multifractal properties but with

492 different $K(q)$ scaling exponents, especially at low and high order moments. This is illustrated by a

493 change in multifractal parameter estimates that is noticeable when compared to the relative

494 homogeneity of the parameters for 5 cm depth data across different stations. A possible explanation

495 could reside in the impact of soil texture on soil moisture at the deeper layers. For instance,

496 subsurface processes could cause a change of the scaling of some moment orders, this change

497 propagating to the multifractal parameters.

498

6 Multiscale entropy properties

6.1 MSE analysis

The nine surface (5 cm depth) soil moisture time series are now analyzed within the MSE framework. For each series, sample entropy is estimated at various coarse resolution time series obtained by the means of averages performed over non-overlapping intervals of various durations τ chosen between 1 h, i.e. the finest resolution available, and 690 h. We cannot degrade the time series to coarser resolutions since the sample entropy calculation can only be performed over coarse time series containing at least 100 points (Nogueira, 2017). The estimated entropies are represented in logarithmic coordinates on Figure 10 for the different time series. Once again, MSE curves are regularly shifted upwards to make the figure more readable. MSE curves are steeper at lower time scales and a bit flatter at larger scales. The segmentation tool proposed by J. D'Errico (2017) was used to estimate the position of the transition between the two behaviors, with a result close to 30 h. Due to the better sampling of the MSE on the right of the figure, only time scales within the range 650 h − 30h have been considered for fitting. The exponents H' are determined by linear regressions over this interval of time scales. The values of H' estimates and error bars may be found in Table 4. Estimates are comprised between 0.31 and 0.66 for a mean value of $H' = 0.43$ for all time series. All the regressions have a very good coefficient of determination except in the case of the Mouthoumet station.

Despite the narrower scale range, the results are partially coherent with the findings previously obtained by spectral analysis, with often similar scaling exponents across stations (see Table 2). Once again, all time series have rather similar scaling properties which could be related to the sampling strategies (all sensors being located in grassland on flat areas). Nevertheless, it could be noted that the dispersion of the values of H' is greater than the dispersion of spectral slopes. This dispersion is nevertheless probably not representative of a better sensitivity of MSE to local differences: indeed, H' is estimated over a significantly narrower scale range than β which could lead to more dispersion in the estimates.

Furthermore, the soil moisture series collected at 10 cm, 20 cm and 30 cm depths have been analyzed in a similar way. The scaling exponents H' obtained by fitting the MSE curves are displayed on Figure 11. All these exponents have been obtained by linear fits on the log-log graph of MSE(τ) for time scales in the range 30h − 650 h (all linear regressions had an R^2 greater than 0.94 except in the case of Peyrusse Grande where the fits are poorer). Figure 11 also confirms that the scaling

530 exponents may depend on depth. Coherently with what was reported on Figure 3, the scaling seems

531 in general a bit steeper at greater depths.

532 The results of this section confirm that the scaling properties of soil moisture may be retrieved not

533 only in terms of spectra and moments, but also in terms of information content. This was expectable

534 since the signal information (occurrence of unexpected structures) is of course strongly constrained

535 by the probability distribution of the signal at various resolutions. Nevertheless, this result shows

536 that multiscale entropy scaling can be found in non-biological natural signals, consistently with the

537 findings by Nogueira (2017). Additionally, our results show that MSE scaling may be found in natural

538 signals that follow multifractal statistics. This could extend the findings of the literature that mainly

539 focuses on monofractal Brownian processes or natural processes assimilated to the former ones (e.g.

540 Gao et al., 2015).

541 Complementarily, we may investigate which degree of redundancy may exist between the MSE

542 approach and the structure function approach, i.e. to check if they estimate the same scaling

543 properties or not. Indeed, first-order structure functions can be used to estimate the third parameter

544 H of the FIF model (cf. Section 2.3). In the case of our dataset, is H indeed close to the MSE scaling

545 parameter obtained above?

6.2 Comparison with first order structure functions

547 In order to investigate this issue, the first-order structure functions (defined by Eq. 4) have been

548 estimated based on the surface soil moisture data from the nine stations. The structure functions are

549 displayed on Figure 12, where they are regularly shifted in the vertical direction to improve

550 readability. It should be noted that on Figure 12, the large time increments are on the right of the

551 figure. Very small and very large time increments are not taken into account as they might be

552 affected by sampling limitations. On the middle of the Figure 12, a scaling regime may be identified

553 for $30\,h \leq \Delta t \leq 1000\,h$. This regime is representative of a scaling behavior of the form given by Eq.

554 5. In order to make the comparison with Sect. 6.1 easier, the linear fit range was restricted to $30\,h \leq$

555 $\Delta t \leq 650\,h$. Good scaling results are obtained, with an very small error bar on the slope estimate (

556 $\Delta H \approx \pm 0.01$ or smaller). The scaling exponent does not vary much from one series to another,

557 the mean value of H being equal to H = 0.41 (see values in Table 5).

558

559 We may now compare the estimates of H and H' obtained for the different series. Figure 13 displays

560 H' as a function of H for the different time series. For most stations, estimates of H and H' are very

561 similar despite some differences larger than the regressions error bars. However, significant

562 differences were found for two stations (Narbonne and Savenès) where the H' estimates are much

563 larger than their structure function counterparts. It remains unclear if this is due to greater

564 uncertainties in the estimates obtained by the MSE approach and/or an ability of the latter method

565 to catch specific features at some stations. This issue could be investigated in future studies since

566 MSE and structure function approaches may perform differently in the estimation of Hurst-like

567 scaling parameters.

568 While the detailed comparison of the two methods still requires additional theoretical work, we can

569 already notice that each method has qualitatively identifiable practical advantages and drawbacks.

570 Namely, classical structure functions are more easy to use to analyze a large scale range but do not

571 have direct interpretation in terms of signal information. Additionally, they cannot estimate negative

572 scaling exponents (unless modified variants based on wavelets are used, e.g., Lovejoy and Schertzer,

573 2012). Meanwhile, MSE algorithms are appropriate for information and complexity estimation but

574 they are applicable over a relatively limited scale range due to computational constraints (Nogueira,

575 2017). The MSE framework also provides equations that seem more difficult to relate analytically to

576 equations such as those governing the statistics of multifractal cascades for non-unity orders of

577 statistics (Eq. 2). It could be interesting to try to investigate possible links with other theoretical

578 notions such as the information dimension, which contains both scaling and (Shannon) entropy

579 characterization. The latter point is left as a perspective in this work. However, a better

580 understanding of the possible relationship between multifractal scaling and MSE scaling can already

581 be achieved with the help of numerical tests. This is the subject of the next section.

582

583

7 Expected relationship between *H'* and multifractal parameters

7.1 Numerical experiments

The analysis presented in Section 6 was aimed to test if *H* and *H'* estimates could have close values in the empirical case of the study. While the hypothesis $H \approx H'$ has been tested numerically by Nogueira (2017) in the case of fractional Brownian motion processes where the structure function *H* is the unique scaling parameter, the extension to the case of multifractal processes has not yet been investigated by theoretical or numerical approaches (at least to the author's knowledge). Multifractal processes differ from fractional Brownian motions by the existence of more nonlinear properties that are characterized by the parameters C_1 and α defined above. A priori, there is no theoretical reason to rule out a possible effect of C_1 and α on the MSE scaling parameter. Therefore, we might look for a possible functional relationship of the form $H' = f(H, C_1, \alpha)$. While it is still unknown if this function f can be defined in closed form, numerical tests can be performed to check if there is a systematic dependency of *H'* on the three multifractal parameters.

In the following, numerical tests are presented based on the multifractal simulation techniques of FIF processes described by (Pecknold et al., 1993; Schertzer and Lovejoy, 2002; Macor, 2007; Verrier, 2011). The main steps are the following: (i) generation of a unit extremal Lévy-stable noise (with an asymmetry parameter equal to -1 and a stability parameter α identical to the multifractal α defined above); (ii) multiplication by a (normalizing) multiplicative constant $\sigma = \left(\frac{C_1}{\alpha-1}\right)^{1/\alpha}$; (iii) Convolution by a kernel proportional to $|t|^{-\frac{D}{\alpha}}$ where *D* is the embedding space dimension (i.e. *D* = 1 for time series); (iv) Exponentiation; (v) fractional integration of order *H*. Step (i) above is performed by applying the procedure described by Chambers et al. (1976) to a couple of independent simple random variables at each data point. It is worth noting the procedure allows to store numerical realizations of these two simple "input" variables *U* and *E* (with uniform and exponential distributions respectively, cf. Pecknold et al., 1993, § 3) and then to repeat the five-step procedure with different sets of parameters (*H*, C_1, α). Therefore, it is very easy to test different sets of parameters on the same probabilistic events (i.e. numerical realizations).

Numerical tests have been implemented in the following way. Twenty independent realizations of couples of *U* and *E* time series are first generated in order to build the experiment on twenty different probabilistic events. Then, the procedure of simulation is applied for various sets of multifractal parameters (*H*, C_1, α) – in other words 20 synthetic multifractal time series are obtained for each set of parameters but the 20 random realizations used to generate the series are the same

21

615 for all sets. Since synthetic multifractal time series can have numerical discrepancies at the highest

616 frequencies, it has been chosen to perform all numerical simulations based on time series of 2^{18}

617 points and then to average each of them over a series of disjoint intervals of 16 points. This

618 procedure provides 20 time series of 2^{14} = 16384 points for each set of multifractal parameters.

619 In a second step, MSE analysis is applied to each individual time series and then the MSE(τ) function

620 is averaged over the 20 individual realizations available for each set of multifractal parameters. The

621 H' exponent is then estimated *from the averaged MSE(τ)* by performing a linear regression in log-log

622 coordinates over the whole range of available scales (i.e. from 1 to 163 data points since sample

623 entropy needs 100 data points to be computed).

624

7.2 Results

626 Examples of MSEs estimated from individual series are presented in log-log coordinates on Figures 14

627 and 15. Figure 14 shows the MSE(τ) obtained for a single random realization with α = 2 and C_1 = 0.05.

628 The blue curve is obtained when H = 0 and the green curve when H has been fixed to 0.4. It may be

629 noticed that the effect of the fractional integration (i.e. transition from the blue to the green curve)

630 changes both the height and the slope of the MSE(τ) function. In this individual case, the hypothesis

631 $H' \approx H$ seems to hold when 0.4, but a moderate scaling is found in the H = 0. Figure 15 illustrate the

632 case where the parameter C_1 changes (while α = 2 and H = 0) based on a different individual

633 realization. The increase of C_1 leads to a drastic decrease of the entropy and seems also to increase

634 the slope H' of the MSE curve.

635 These conclusions are globally confirmed when considering the H' estimates obtained from the

636 averaged MSEs (Figs. 16-17). Figure 16 shows the H' estimate as a function of H, with variable C_1

637 while α is fixed to 2. On the figure, each curve corresponds to one value of C_1 comprised between

638 0.05 (continuous blue curve) and 0.55 (dashed green curve) with a spacing of 0.10. H is sampled in

639 the range [0, 0.7] with a spacing of 0.10. The first bisectrix is represented as a dashed black line. For

640 all curves, H' increases with H but does not follow the bisectrix (except when C_1 is very small). When

641 H > 0.5, all curves tends to get relatively close to each other meaning that when H is sufficiently high,

642 the influence of C_1 on H' is relatively small. On the contrary, when H < 0.4, the influence can become

643 quite large with a systematic increase of H' with C_1 (confirming the observation of Figure 15). In the

644 case of a non integrated multiplicative cascade (H = 0), this can lead to an H' estimate varying within

645 the range [0.1; 0.3] depending on the C_1 value. Regression error bars on H' estimated from the

646 average MSE(τ) functions are not represented because they are very small (inferior to 0.01).

647 The possible influence of the α parameter (coupled with H) is presented on Figure 17, where H' is

648 represented as a function of H, with one curve for one value of α (C_1 being fixed to 0.25). The

649 parameter α has been chosen in the interval [1.5, 2] with a spacing of 0.1 (i.e., values usually

650 encountered in geophysics, and also reported in this study). Again, H' is an increasing function of H

651 for all curves which also remain above the first bisectrix. However, H' is a decreasing function of α

652 such that the relationship between H' and H tends to become closer to the first bisectrix when α = 2.

653 We may notice that the dependency of H' on α is very limited for high values of α (α > 1.7) but

654 becomes more pronounced for smaller values. Finally, we may again notice that for high values of H,

655 all curves become close to the first bisectrix and increasingly undistinguishable from each other (e.g.,

656 $H = 0.7$).

657 These numerical results show that the relationship between multifractal parameters and the MSE

658 scaling properties is more complex than originally anticipated and that a dependency on the three

659 multifractal parameters should be expected in the general case. However, we may distinguish two

660 basic cases:

661 • For relatively high values of H (> 0.4-0.5), the relationship $H \approx H'$ might still provide a useful

662   work assumption since our results suggest that the fractional integration washes out the

663   possible effects of the multifractal parameters α and C_1. In this case, the MSE scaling

664   properties of a multifractal process are expectedly close to those of a fractional Brownian

665   motion which have been investigated by Nogueira (2017).

666 • For lower values of H, and in particular in the case of a non-integrated multiplicative cascade

667   ($H = 0$), the effect of α and C_1 is visible and results in a MSE scaling exponent that is higher

668   than H (i.e. $H' = H + g(H, C_1, \alpha)$). The positive offset modeled by the function g is higher when

669   C_1 increases or when α becomes significantly smaller than 2. Interestingly, the offset

670   becomes very small when C_1 takes small values, which illustrates that multifractal

671   intermittency plays an important role in the difference $H'-H$.

672 While more exhaustive numerical tests and theoretical work remain to be done to quantify and

673 understand the relationships between multifractal parameters and observed MSE scaling laws, some

674 qualitative arguments may help to interpret the present observations. First, the effect of the

675 fractional integration included in the FIF model is similar to a (scaling) low-pass filter that significantly

676 attenuates the variability at the smallest scales. It is therefore expectable that a fractionally

677 integrated signal ($H > 0$) possesses more entropy at coarse resolutions than at fine resolutions. This is

678 obvious on Figure 14 where we see that the effect of H is to strongly reduce entropy estimates at

679 small scales (i.e. on the left part of Fig. 14). Moreover, as already noted on Figure 15, high C_1

680   parameter values also contribute to strongly reduce entropy. This could seem a bit paradoxical since

681   C_1 is known as an intermittency/heterogeneity parameter. However, multifractal processes with high

682   C_1 correspond to processes that exhibit slow variations most of the time, while most of the variance

683   is due to very strong and sparse peaks (e.g., fig. 10 in Pecknold et al., 1993). In this case, sample

684   entropies tend to decrease since repetitive patterns are (or seem) more frequent due to the

685   existence of wide areas with small variations. This effect is even more pronounced due to the

686   increased standard deviation of the process when C_1 is large due to the contribution of extreme

687   peaks. Indeed, since the sample entropy builds its similarity criterion by using the standard deviation

688   of the series (see Eq. 6), it classifies events as similar more easily when large standard deviation and

689   C_1 are involved. We can notice that the decrease of entropy is expectably stronger at small scales

690   where peaks are both very intense and cover a very small fraction of the time.

691   **7.3 Application to SMOSMANIA empirical parameters**

692   Finally, we may come back to the results of Section 6 since we have just demonstrated that the initial

693   hypothesis $H \approx H'$ may be too simplistic for multifractal processes in some situations. By reporting the

694   parameters (H, C_1, α) estimated in Sections 5 and 6.2 to the graph presented on Figure 17, we obtain

695   an expected parameter H' between 0.4 and 0.5. However, the empirical H' estimates found in Section

696   6.1 ($\approx$ 0.40) are less coherent with this expected parameter ($H' \approx$ 0.47-0.48 for multifractal

697   parameters α = 1.7, C_1 = 0.25, H = 0.40) than the one resulting from the naive $H \approx H'$ hypothesis.

698   Beyond possible estimation uncertainties, a plausible explanation for this observation is the fact that

699   the multifractal parameters C_1 and α are expected to be valid in the range of scales 128h – 1 h, while

700   H and H' are valid in the range 650 h – 30 h. At scales larger than 128 h (i.e., beginning of the

701   "macroweather" regime), the flux moments have much slower variation with scale (Figs. 4-5), which

702   is equivalent to a strong decrease of the C_1 parameter. This could explain why the empirical

703   estimates of H' are close to the structure function exponents since it is what is expected for low

704   values of C_1 (see Figure 16, continuous blue curve), especially when H is still relatively large (0.4 in

705   this case).

706

707

708   # 8 Conclusions

709   Like other geophysical processes, soil moisture is strongly variable over a rather wide range of time

710   (and space) scales. Some previous literature papers advocated the existence of scaling and fractal

properties over various ranges of scales. In this study, 8-year time series of surface soil moisture have been analyzed with the help of various multiscale analysis tools in order to investigate the existence of scaling laws. The twelve sensors are located in the same area of about 300 x 200 km² in southwestern France and the average distance between stations is of the order of a few dozens of kilometers. For nine of these stations, power spectra of surface soil moisture showed a red noise-like $1/f^2$ scaling over a large scale range of time scales (1 h ≤ τ ≤ 1000 h), without any strong break in the scaling. The scaling exponents are rather homogeneous at the surface layer and exhibit some variability at deeper horizons where spectra tend to become steeper.

In a second step, multifractal analysis has been applied in order to identify the possible existence of scaling properties for non-quadratic moment orders. Multifractality has also been observed in the range of scales comprised between 1 h and 128 h. The moment scaling functions have been successfully fitted with the two-parameter functional form predicted by the Universal Multifractal Model. At the surface (5 cm depth) layer, the obtained parameters showed a slightly greater dispersion than that of spectral slopes, with $C_1 \approx 0.2$-0.3 and $\alpha \approx 1.3$-1.8 for surface data (5 cm depths). However, a greater dispersion has been found for data collected at deeper horizons (10-30 cm). On average, the depth affects the multifractality parameters more strongly than spectral slopes. At 30 cm depth, C_1 is closer to 0.4-0.5 while α often becomes smaller than 1. This shift and this variability could be related to the soil composition while surface parameters are likely to be more representative of the influence of the meteorological forcing.

Multiscale entropy has also been applied as a complementary scaling analysis tool devoted to the multiscale analysis of information content present in the series. This approach had been originally developed in Biology/medicine research literature and has a good potential for analyzing time series in other scientific fields. As noticed by Nogueira (2017), a systematic relationship exists between MSE scaling and spectral/first-order structure function scaling in the case of synthetic monofractal data and seems to hold for scaling geophysical observations.

MSE analysis has been performed over the twelve SMOSMANIA surface time series, showing the existence of scaling properties for the sample entropies estimated at various aggregation resolutions (30-650 hours). Due to the strong constraints on sample entropy estimation, the validity of MSE scaling at larger scales could not be investigated. This is a basic (methodological) limitation of the MSE approach that is compensated by other advantages: contrary to the usual structure function approach, MSE could be appropriate to analyze processes with negative Hurst scaling exponents (i.e. with $H < 0$ or $\beta < 1$) and has a rather direct interpretation in terms of information theory.

743   More generally, our numerical results also demonstrated that the MSE scaling properties are not

744   limited to fBm-like *monofractals* investigated by previous authors (Gao et al., 2015; Nogueira, 2017)

745   but should hold for synthetic and natural signals characterized by *multifractal* properties. Numerical

746   tests were used to investigate the existence of a systematic relationship between the MSE scaling

747   parameter H' and the three multifractal parameters H, C_1 and α. It has been observed that the

748   relationship $H' = f(H, C_1, \alpha)$ is more complex than in the monofractal case (where $H' \approx H$) and that in

749   some cases the intermittency parameter C_1 and the multifractality parameter α can affect

750   significantly MSE scaling properties. In other cases (i.e. large H or low intermittency), the

751   approximation $H' \approx H$ could be acceptable. Finally, more theoretical work remains to be done to

752   understand the relationships between MSE scaling and fractal/multifractal scaling properties. This

753   could open interesting perspectives for a better physical understanding of many geophysical

754   processes that exhibit multifractal properties.

755

756

757   **Acknowledgements**

761

762

763

References

Albergel, C., Rüdiger, C., Calvet, J.-C., Carrer, D., Fritz, N., Pellarin, T., 2010 (in French). Utilisation de mesures in situ d'humidité des sols pour l'évaluation de produits satellitaires micro-ondes dans le Sud-Ouest de la France. La Houille Blanche, 2, 120-126. doi : 10.1051/lhb 2010027.

Albergel, C., Zakharova, E., Calvet, J.-C. et al., 2011. A first assessment of the SMOS data in southwestern France using in situ and airborne soil moisture estimates: The CAROLS airborne campaign. Remote Sensing of Environment 115, 2718-2728. doi:10.1016/j.rse.2011.06.012.

Calvet, J.-C., Fritz, N., Froissard, F., Suquia, D., Petitpa, A., Piguet, B. 2007. In situ soil moisture observations for the CAL/VAL of SMOS: the SMOSMANIA network. Proceedings of the International Geoscience and Remote Sensing Symposium, IGARSS, Barcelona. doi:10.1109/IGARSS.2007.4423019.

Chambers, J.M., Mallows, C.L., Stuck, B.W., 1976. A method for simulating stable random variables. J. Amer. Statist. Assoc., 71, 340-344.

Corrsin, S., 1951. On the spectrum of isotropic temperature fluctuations in an isotropic turbulence. J. Appl. Phys. 22, 469–473.

Costa, M., Goldberger, A.L., Peng, C.K. , 2002. Multiscale entropy analysis of complex physiologic time series. Phys. Rev. Lett. 2002, 89. https://doi.org/10.1103/PhysRevLett.89.068102.

Costa, M., Peng, C.K., Goldberger, A.L. Haussdorff, J.M., 2003. Multiscale entropy analysis of human gait dynamics. Physica A 330, 53-60. doi:10.1016/j.physa.2003.08.022.

Costa, M., Goldberger A.L., Peng C.K., 2005. Multiscale entropy analysis of biological signals. Phys. Rev. E. 2005; 71: 021906. DOI: 10.1103/PhysRevE.71.021906

Courtiol, J., Perdikis, D., Petkoski, S., Muller, V., Huys, R., Sleimen-Malkoun, R., Jirsa, V.K., 2016. The multiscale entropy: Guidelines for use and interpretation in brain signal analysis. J. Neuro. Meth. 2016; 273: 175-190.

D'Errico, J., (2017). SLM – Shape Language Modelling Toolbox, accessible at: http://mathworks.com/matlabcentral/fileexchange/24443-slm-shape-language-modeling.

de Lima, M.I. P., Lovejoy, S., 2015. Macroweather precipitation variability up to global and centennial scales, Water Resour. Res., 51, 9490-9513. doi:10.1002/2015WR017455.

Dorigo, W. A., Wagner, W., Hohensinn, R., Hahn, S., Paulik, C., Xaver, A., Gruber, A., Drusch, M., Mecklenburg, S., van Oevelen, P., Robock, A., and Jackson, T., 2011. The International Soil Moisture Network: a data hosting facility for global in situ soil moisture measurements, Hydrol. Earth Syst. Sci., 15, 1675-1698, doi:10.5194/hess-15-1675-2011.

Entekhabi, D., Njoku, E.G., et al., 2010. The Soil Moisture Active Passive (SMAP) mission. Proceedings of the IEEE, 10.1109/JPROC.2010.2043918.

Farmer, J.D., Ott, E., Yorke, J.A., 1983. The dimension of chaotic attractors. Physica D: Nonlinear Phenomena, 7, issues 1-3, 153-180.

799

800   Fraedrich, K., Larnder, C., 1993. Scaling regimes of composite rainfall time series, Tellus, 45, 289-298.

801   Gagnon, J.S., Lovejoy, S., Schertzer, D., 2006. Multifractal Earth Topography. Nonlin. Processes
802   Geophys. 13, 541-570.

803   Gao, J., Hu, J., Liu, F., Cao, Y., 2015. Multiscale entropy analysis of biological signals: a fundamental
804   bi-scaling law. Front. Comput. Neurosci. 2015, 9: 64. https://doi.org/10.3389/fncom.2015.00064 .

805   Gires, A., Onof, C., Maksimovic, C., Schertzer, D., Tchiguirinskaia, I., Simoes, N., 2012. Quantifying the
806   impact of small scale unmeasured rainfall variability on urban runoff through multifractal
807   downscaling: A   case   study.   Journal   of   Hydrology,   442-443,   117-128,
808   http://dx.doi.org/10.1016/j.jhydrol.2012.04.005.

809   Hentschel, H.G.E. , Procaccia, I., 1983. The infinite number of generalized dimensions of fractals and
810   strange attractors. Physica D, 8 (3), 435-444.

811   Katul, G., Porporato, A., Daly E., Oishi, C., Kim, H.-S., Stoy, P.C., Juang, J.Y., Siquira, M.B., 2007. On the
812   spectrum of soil moisture from hourly to interannual scales. Water Resources Research, 43, W05428,
813   doi:10.1029/2006WR005356.

814   Kerr, Y., Waldteufel, P., et al. 2010. The SMOS mission : new tool for monitoring key elements of the
815   global water cycle. Proceedings of the IEEE, 98, 666–687. doi: 10.1109/JPROC.2010.2043032.

816   Kerr, Y., Al-Yaari, A., et al., 2016. Overview of SMOS performance in terms of global soil moisture
817   monitoring after six years in operation. Remote Sensing of Environment 180, 40-63.
818   http://dx.doi.org/10.1016/j.rse.2016.02.042.

819   Kim, G., Barros, B., 2002a. Space–time characterization of soil moisture from passive microwave
820   remotely sensed imagery and ancillary data. Remote sensing of Environment 81, 393-403.

821   Kim, G., Barros, B., 2002b. Downscaling of remotely sensed soil moisture with a modified fractal
822   interpolation method using contraction mapping and ancillary data. Remote sensing of Environment
823   83, 400-413.

824   Kolmogorov, A.N., 1941. Local structure of turbulence in an incompressible liquid for very large
825   Reynolds numbers. Proc. Acad. Sci. URSS, Geochem. Sect. 30, 299–303.

826   Lavallée, D., 1991. Multifractal Techniques: Analysis and Simulation of Turbulent Fields. Ph. D. Thesis,
827   McGill University, Montréal, Canada.

828   Lavallée, D., Lovejoy, S., Schertzer, D., Ladoy, P., 1993. Nonlinear variability of landscape topography:
829   multifractal analysis and simulation. In: De Cola, L., Lam, N. (Eds.), Fractals and Geography. Prentice
830   Hall, New Jersey, pp. 158–192.

831   Lovejoy, S., Schertzer, D., 2006. Multifractal, cloud radiances and rain. Journal of Hydrology, 322, 59-
832   88, doi:10.1016/j.hydrol.2005.02.042.

833 Lovejoy, S., Schertzer, D., 2010. Towards a new synthesis for atmospheric dynamics: space-time
834 cascades. Atmospheric Research, 96, 1-52. https://doi.org/10.1016/j.atmosres.2010.01.004

835 Lovejoy S., Schertzer D., 2012. Haar wavelets, fluctuations and structure functions: convenient
836 choices for geophysics. Nonlin. Proc. Geophys., 19, 513-527.

837 Lovejoy, S., and Schertzer, D., 2013. The Weather and Climate: Emergent Laws and Multifractal
838 Cascades, 496 pp., Cambridge University Press.

839

840 Lovejoy, S., Schertzer, D., Allaire, V., 2008. The remarkable wide range spatial scaling of TRMM
841 precipitation. Atmos. Res. 90, 10–32.

842 Lovejoy, S., Tarquis, A.M., Gaonac'h, H., Schertzer, D.,2008. Single- and multiscale remote sensing
843 techniques, multifractals, and MODIS-derived vegetation and soil moisture. Vadose Zone J. 7: 533–
844 546.

845 Lovejoy, S., Schertzer, D., Varon, D., 2013. Do GCMs predict climate… or macroweather? Earth Syst.
846 Dyn., 4, 439-454, doi:10.5194/esd-4-439-2013.

847 Loverro, A., 2004. Fractional calculus: history, definitions and applications for engineer. USA:
848 Department of Aerospace and Mechanical Engineering, University of Notre Dame; 2004.p. 870–84.

849 Macor, J.L., 2007. Développement de techniques de prévision de pluie basées sur les propriétés
850 multi-échelles des données radar et satellite. PhD Thesis (in French), Ecole Nationale des Ponts et
851 Chaussées, Marne-la-Vallée, France.

852 Mandelbrot, B. B.: The Fractal Geometry of Nature, Freeman, NewYork, 1983.

853 Mascaro, G., Vivoni, E.R., 2010. Statistical and scaling properties of remotely-sensed soil moisture in
854 two contrasting domains in the North American monsoon region. J. Arid Environ. 74: 572–578.
855 doi:10.1016/j.jaridenv.2009.09.023.

856 Mascaro, G., Vivoni, E.R., 2012. Comparison of statistical and multifractal properties of soil moisture
857 and brightness temperature from ESTAR and PSR during SGP99. IEEE Geosci. Remote Sens. Lett. 9:
858 373–377. doi: 10.1109/LGRS.2011.2169770.

859 Mascaro, G., Vivoni, E.R., Deidda, R., 2010. Downscaling soil moisture in the southern Great Plains
860 through a calibrated multifractal model for land surface modeling applications. Water Resour. Res.
861 46. W08546, doi:10.1029/2009WR008855.

862 Mascaro, G., Vivoni, E.R., Deidda, R., 2011. Soil moisture downscaling across climate regions and its
863 emergent properties. J. Geophys. Res. (Atm.) 116. D22114, doi:10.1029/2011JD016231.

864 Merlin, O., Walker, J.P., Chehbouni, A., Kerr, Y., 2008. Towards deterministic downscaling of SMOS
865 soil moisture using MODIS derived soil evaporative efficiency. Remote Sensing of Environment, 112,
866 3935-3946. doi: 10.1016/j.rse.2008.06.012

867 Merlin, O., Rüdiger, C., Al Bitar, A., Richaume, P., Walker, J., Kerr, Y., 2012. Disaggregation of SMOS
868 soil moisture in southeastern Australia. IEEE Transactions on Geoscience and Remote Sensing, 50,
869 1556-1571. doi: 10.1109/TGRS.2011.2175000

870 Neuhauser, M., Verrier, S., Mangiarotti, S., 2018. Propriétés statistiques multi-échelles de produits
871 satellitaires SMOS d'humidité du sol désagrégés à la résolution kilométrique (in French). Proc. of
872 Rencontres du Non-Linéaire 2018, Paris, France.

873 Nogueira, M., 2017. Exploring the link between multiscale entropy and fractal scaling behavior in
874 near-surface wind. PLoS ONE 12(3):e0173994. https://doi.org/10.1371/journal.pone.0173994.

875 Obukhov, A.M., 1949. Structure of the temperature field in a turbulent flow. Izv. Akad. Nauk S.S.S.R,
876 Ser Geograf. Geofiz. 13, 58–69.

877 Olsson, J., 1995. Limits and characteristics of the multifractal behaviour of a high-resolution rainfall
878 time series. Nonlin. Proc. Geophys., 2(1), 23-29.

879 Pandey, G., Lovejoy, S., Schertzer, D., 1998. Multifractal analysis of daily river flows including
880 extremes for basins of five to two million square kilometers, onde day to 75 years. Journal of
881 Hydrology 208, 62-81.

882 Pelletier, J.D., Malamud, B.D., Blodgett, T., Turcotte, D.L., 1997. Scale-invariance of soil moisture
883 variability and its implicationsfor the frequency-size distribution of landslides. Engineering Geology
884 48, 255-268.

885 Richman, J.S., Moorman, J.R.,2000. Physiological time-series analysis using approximate entropy and
886 sample entropy. Am. J. Physiol. Heart. Circ. Physiol. 2000; 278: H2039-H2049

887 Schertzer, D., Lovejoy, S., 1987. Physical modelling and analysis of rain and clouds by anisotropic
888 scaling multiplicative processes. J. Geophys. Res. 92 (D8), 9693–9714.

889 Schertzer, D., Lovejoy, S., 1991. Nonlinear geodynamical variability: multiple singularities, universality
890 and observables. In: Nonlinear Variability in Geophysics, D. Schertzer and S. Lovejoy (eds.), Kluwer,
891 Netherlands, 1991, p. 41-82.

892 Schertzer, D., Lovejoy, S., 1997. Universal multifractals do exist! J. Appl. Meteorol.,36, 1296–1303.

893 Schertzer, D., Lovejoy, S., Hubert, P., 2002. An introduction to stochastic multifractal fields. In: Ern,
894 A., Weiping, L. (Eds.), Mathematical Problems in Environmental Science and Engineering. Series in
895 Contemporary Applied Mathematics, vol. 4. Higher Education Press, Beijing, pp. 106–179.

896 She Z. S., Levêque, E. (1994), Universal scaling laws in fully developed turbulence, Phys. Rev. Lett., 72,
897 336–339.

898 Tessier, Y., Lovejoy, S., Schertzer, D., 1993. Universal multifractals in rain and clouds: theory and
899 observations. J. Appl. Meteorol. 32, 223–250

900 Vereecken, H., Huisman, J.A., Pachepsky, Y., Montzka, C., van der Kruk, J., Bogena, H., Weihermüller,
901 L., Herbst, M., Martinez, G., Vanderborght, J., 2014. On the spatio-temporal dynamics of soil

902 moisture at the field scale. Journal of Hydrology 516, 76-96.
903 http://dx.doi.org/10.1016/j.jhydrol.2013.11.061

904 Verrier, S., Mallet, C., and Barthès, L. (2011), Multiscaling properties of rain in the time domain,
905 taking into account rain support biases. Journal of Geophysical Research, 116, D20119,
906 http://dx.doi.org/10.1029/2011JD015719.

907 Verrier, S., Crépon, M., Thiria, S. (2014), Scaling and stochastic cascade properties of NEMO oceanic
908 simulations and their potential value for GCM evaluation and downscaling, J. Geophys. Res. Oceans,
909 119, 6444–6460, doi:10.1002/2014JC009811.

910 Zhang, Y.C., 1991. Complexity and 1/f noise. A phase space approach. J. Phys. I. 1991, 1(7): 971-977.

911

912

913

Tables

Station	GPS coordinates (Lat/Lon)		Altitude (m)	Sensor
Condom	43.97440	0.33610	174	ThetaProbe-ML2X
Créon d'Armagnac	43.99360	-0.04690	149	ThetaProbe-ML2X
Lahas	43.54720	0.88780	249	ThetaProbe-ML2X
Lézignan Corbieres*	43.17330	2.72830	60	ThetaProbe-ML2X
Montaut	43.19220	1.64360	295	ThetaProbe-ML2X
Mouthoumet	42.96000	2.53000	538	ThetaProbe-ML2X
Narbonne	43.15000	2.95670	112	ThetaProbe-ML2X
Peyrusse Grande	43.66640	0.22170	245	ThetaProbe-ML2X
Sabres*	44.14750	-0.84560	81	ThetaProbe-ML2X
St Félix de Lauragais*	43.44170	1.88000	337	ThetaProbe-ML2X
Savenès	43.82500	1.17670	158	ThetaProbe-ML2X
Urgons	43.63970	-0.43500	145	ThetaProbe-ML2X

Table 1a : Identification of the 12 SMOSMANIA stations located in the region of interest. Names marked with a star correspond to stations that are not used in the rest of the study.

Station	Soil texture
Condom	Clay
Créon d'Armagnac	Sand
Lahas	Clay
Lézignan Corbieres	Silt loam
Montaut	Silt loam
Mouthoumet	Silt loam
Narbonne	Silt loam
Peyrusse Grande	Clay
Sabres	Sand
St Félix de Lauragais	Clay
Savenès	Silt loam
Urgons	Silt loam

Table 1b : Soil texture classification (in terms of USDA texture classification), based on ISMN/SMOSMANIA metadata information.

925

Station	β	Δβ	R²
Condom	1.99	0.037	0.988
Créon d'Armagnac	2.01	0.037	0.988
Lahas	1.96	0.039	0.987
Montaut	1.97	0.034	0.990
Mouthoumet	2.02	0.036	0.989
Narbonne	1.91	0.034	0.989
Peyrusse Grande	1.93	0.031	0.991
Savenès	1.92	0.030	0.992
Urgons	1.99	0.036	0.989

926

927 **Table 2: Estimates of spectral scaling exponents β for the time series collected at 5 cm depth. Δβ is**
928 **half of the length of the 95% confidence interval on β while the last column presents the**
929 **coefficient of determination.**

930

Station	C_1	α	Validity conditions
Condom	0.22	1.82	$q \leq 2.5$; scales 1-128 h
Créon d'Armagnac	0.26	1.42	«
Lahas	0.27	1.82	«
Montaut	0.31	1.60	«
Mouthoumet	0.22	1.76	«
Narbonne	0.31	1.61	«
Peyrusse Grande	0.28	1.51	«
Savenès	0.27	1.68	«
Urgons	0.29	1.37	«

931

932 **Table 3: Universal multifractal parameter estimates for the nine SMOSMANIA time series collected**
933 **at 5 cm depth.**

934

Station	H'	$\Delta H'$	R^2
Condom	0.31	0.02	0.96
Créon d'Armagnac	0.45	0.02	0.99
Lahas	0.35	0.02	0.98
Montaut	0.38	0.02	0.98
Mouthoumet	0.35	0.04	0.90
Narbonne	0.66	0.02	0.99
Peyrusse Grande	0.36	0.02	0.96
Savenès	0.61	0.01	0.99
Urgons	0.36	0.01	0.98

Table 4: MSE scaling parameter estimates over the time scale range 30 h – 650 h for the nine series collected at 5 cm depth.

Station	H	ΔH	R^2
Condom	0.42	< 0.01	0.98
Créon d'Armagnac	0.37	"	0.97
Lahas	0.41	"	0.98
Montaut	0.41	"	0.99
Mouthoumet	0.39	"	0.96
Narbonne	0.38	"	0.93
Peyrusse Grande	0.39	"	0.98
Savenès	0.47	"	0.99
Urgons	0.42	"	0.99

Table 5: Structure function scaling parameter estimates over the time scale range 30 h – 650 h for the nine stations (surface moisture).

Figures captions

Figure 1: Power spectral densities $E(f)$ of the nine selected SMOSMANIA surface (5 cm depth) soil moisture series in logarithmic coordinates. In order to facilitate the understanding in terms of time scales, the horizontal axis exhibits values of $1/f$ (time scale equivalent to a Fourier frequency). The horizontal axis is presented so that high frequencies (i.e., small time scales) appear on the right of the figure. *The different curves have regularly been translated upwards in order to improve readability*.

Figure 2a: Power spectra of soil moisture at Peyrusse Grande, one spectrum per depth.

Figure 2b: Power spectra of soil moisture at Montaut, one spectrum per depth.

Figure 3: Estimates of spectral slope β for all stations and depths. Each line is associated to a depth. On the abscissa axis, the three letters identify the stations. Stations are sorted from west to east.

Figure 4: Flux moments estimated for the Peyrusse Grande time series of surface soil moisture. Logarithmic scales are used. Moment orders q vary between 0 and 2.5.

Figure 5: Flux moments estimates for the eight other surface soil moisture series. Again, moments orders comprised between 0 and 2.5 are represented.

Figure 6: Moment scaling function $K(q)$ of Peyrusse Grande surface soil moisture series.

Figure 7: Moments scaling functions $K(q)$ estimated for the eight other SMOSMANIA surface soil moisture series.

Figure 8: (**Upper figures and bottom left**) Moments estimations based on Peyrusse Grande data at depths 10, 20 and 30 cm. (**Bottom right**) Moments scaling functions estimated from depths 5, 10, 20 and 30cm.

Figure 9a: estimates of the index of multifractality α for the different stations and depths. Each line is associated to a depth. On the abscissa axis, the three letters identify the stations. Stations are sorted from west to east.

Figure 9b: estimates of the inhomogeneity parameter C_1 for the different stations and depths. Each line is associated to a depth. On the abscissa axis, the three letters identify the stations. Stations are sorted from west to east.

Figure 10: MSE analysis for the nine surface soil moisture series. For each series, the Sample Entropy (SampEn) is estimated for different time resolutions obtained by time aggregation. *Plots are shifted vertically from one station to one another to improve readability*.

Figure 11: MSE scaling parameter estimates over the time scale range 30 h – 650 h for the nine stations and the four depths considered.

Figure 12: First-order structure functions obtained for the nine SMOSMANIA series. *Plots are shifted vertically in order to improve readability.* The different curves are sorted in the same order as in Figure 10 (from Condom at the bottom to Urgons at the top).

Figure 13: Comparison of scaling exponents H and H' provided by SF and MSE methods.

Figure 14: MSE analysis for two synthetic multifractal time series generated with $H = 0$ (blue curve) and $H = 0.4$, for the same random realization. C_1 and α are respectively fixed to 0.05 and 2. Note that contrary to Figs. 1, 2 and 12, no vertical shift is applied here between both curves.

Figure 15: MSE analysis for two synthetic multifractal time series generated with $C_1 = 0.05$ (blue curve) and $C_1 = 0.35$, for the same random realization. H and α are respectively fixed to 0 and 2.

Figure 16: Estimated scaling parameter H' from the MSE analysis averaged on 20 random realizations. α is equal to 2 in these simulations. Each curve represents the evolution of H' as a function of H for a fixed C_1. The values of C_1 are the following: 0.05 (continuous blue curve), 0.15 (dashed blue curve), 0.25 (continuous red curve), 0.35 (dashed red curve), 0.45 (continuous green curve), 0.55 (dashed green curve). H is sampled from 0 to 0.7 with 0.1 spacing.

Figure 17: Estimated scaling parameter H' from the MSE analysis averaged on 20 random realizations. C_1 is equal to 0.25 in these simulations. Each curve represents the evolution of H' as a function of H for a fixed α. The values of α are the following: 1.5 (continuous blue curve), 1.6 (dashed blue curve), 1.7 (continuous red curve), 1.8 (dashed red curve), 1.9 (continuous green curve), 2 (dashed green curve). H is sampled from 0 to 0.7 with 0.1 spacing.

Power spectrum of surface soil moisture data

From top to bottom:
Urgons - Savenès - Peyrusse
Narbonne - Mouthoumet - Montaut
Lahas - Créon - Condom
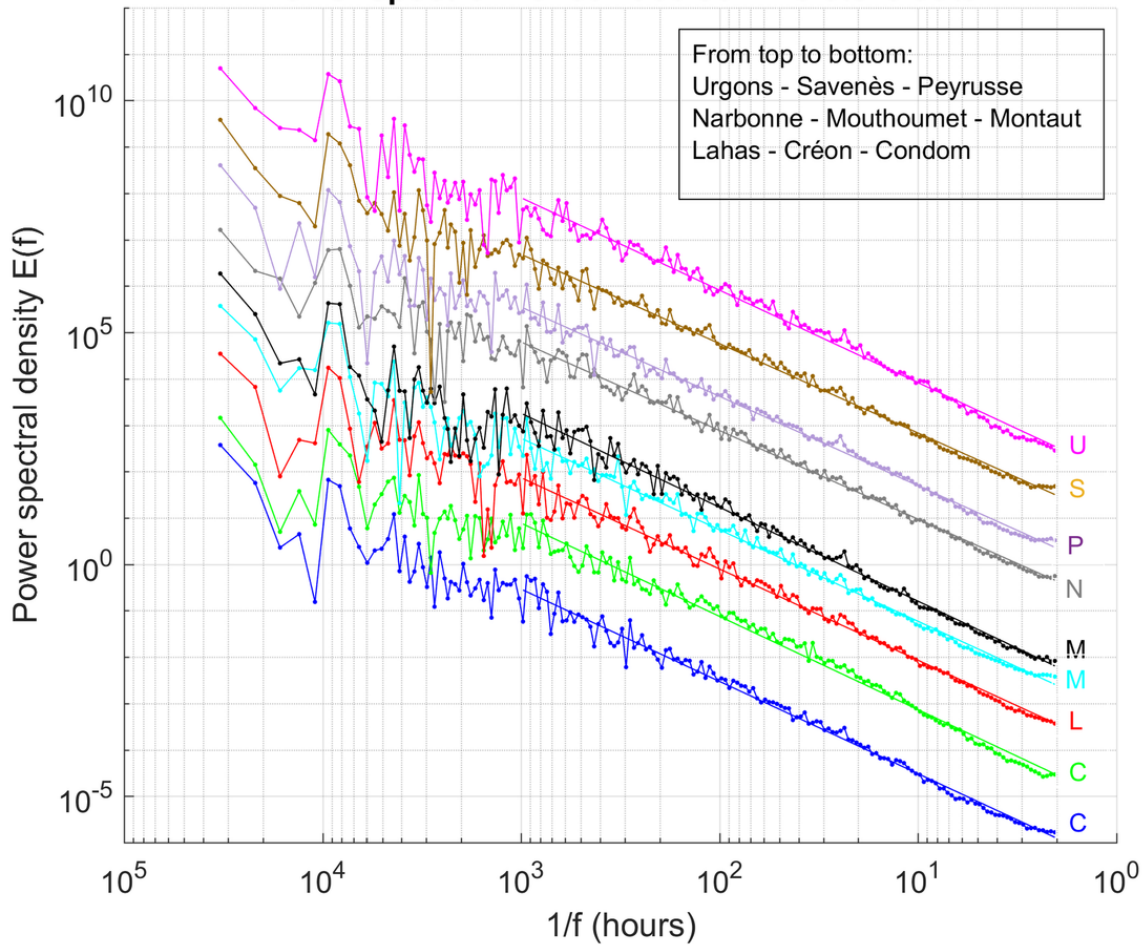
Power spectra of Peyrusse Grande time series
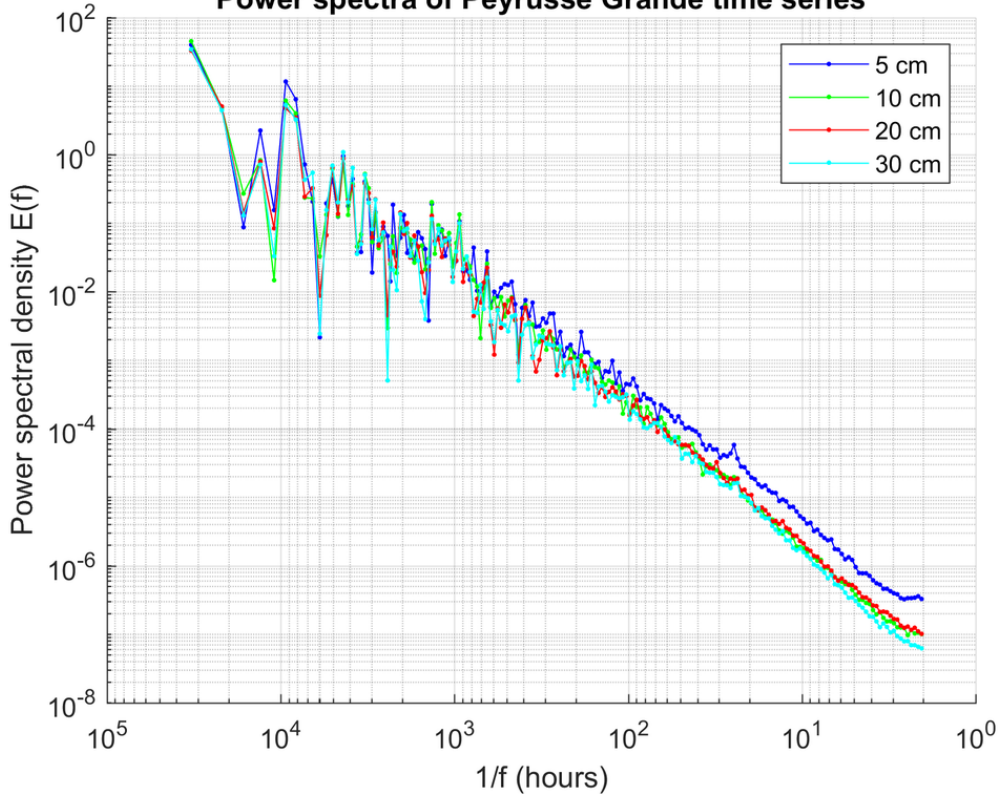
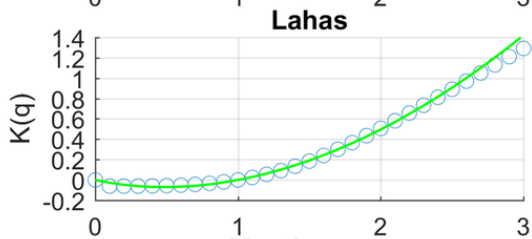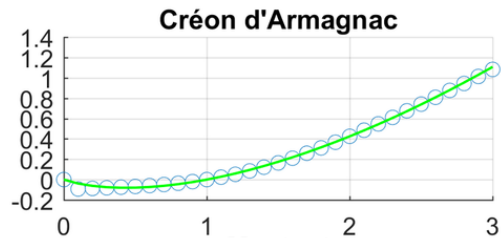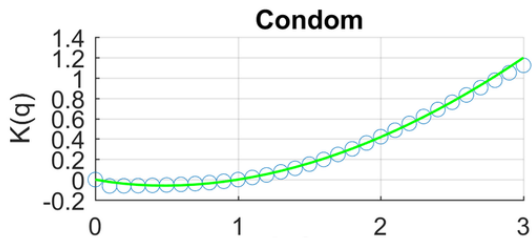Power spectra of Montaut time series
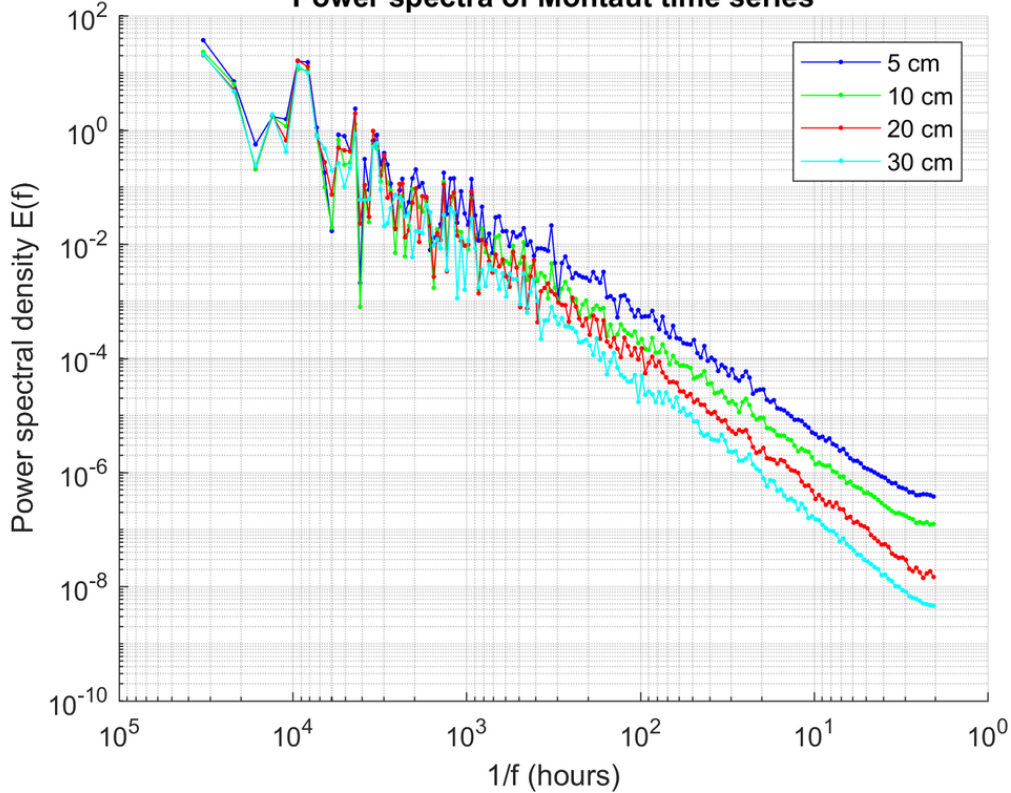
Spectral exponents β for all time series
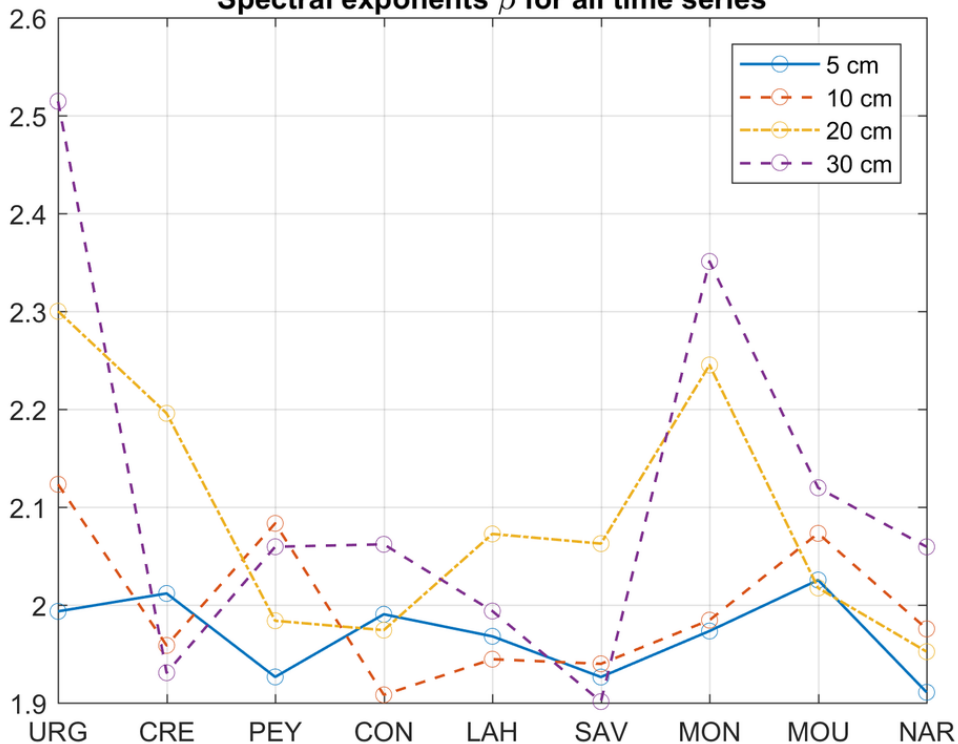
Peyrusse Grande: Moment figure

Condom   Créon d'Armagnac

Lahas   Montaut

Mouthoumet   Narbonne

Savenes   Urgons

Aggregation scale (h)
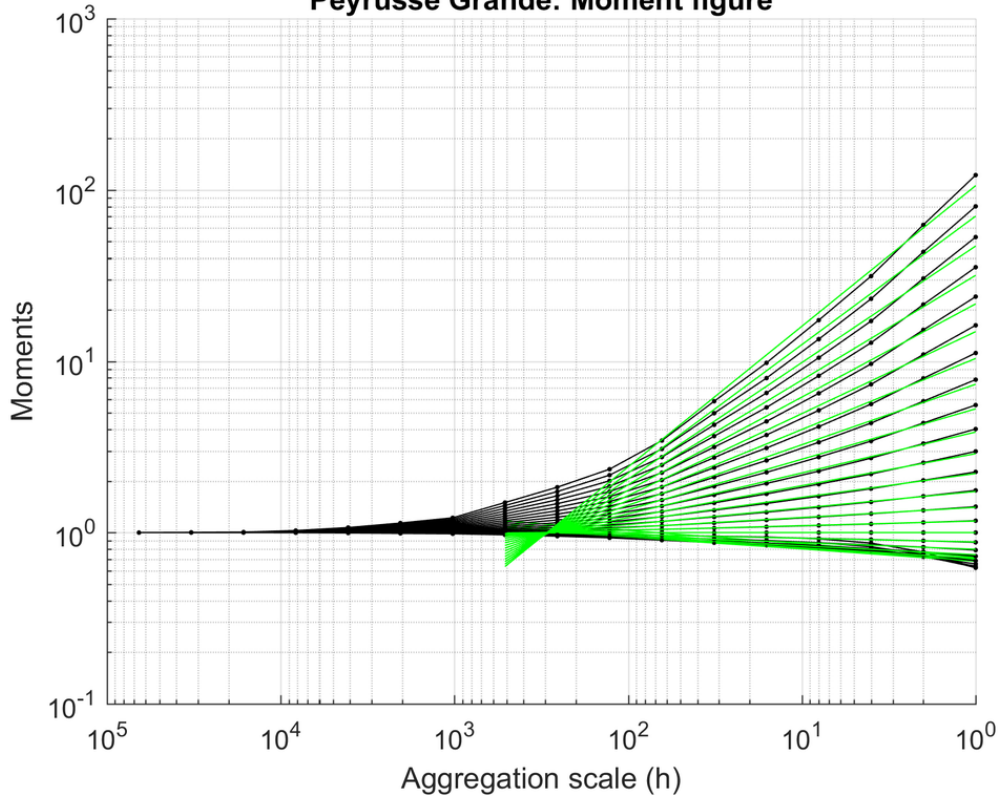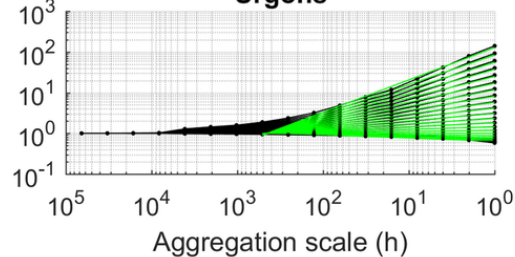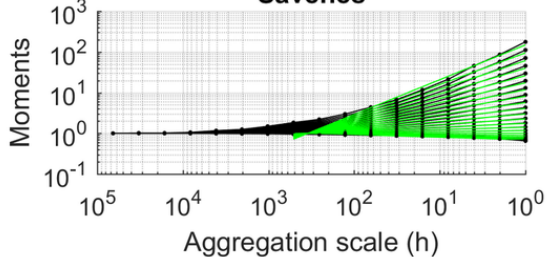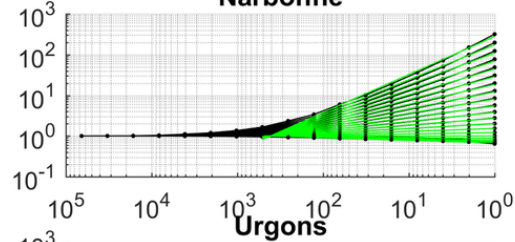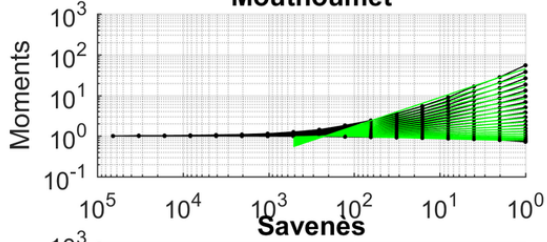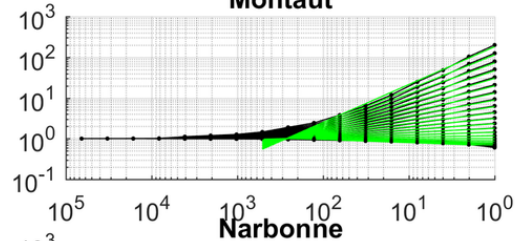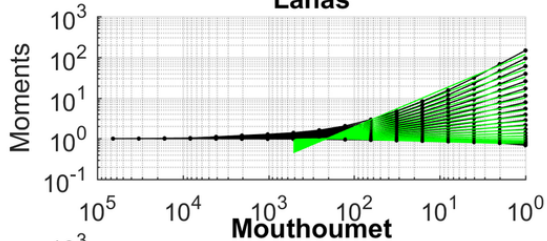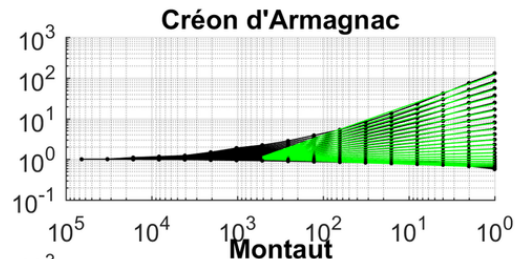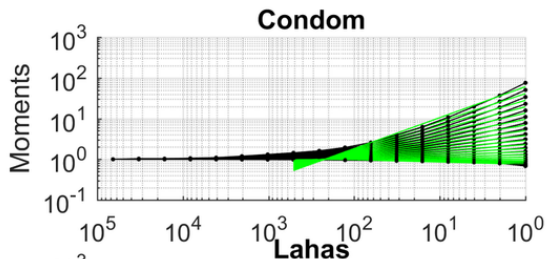
Peyrusse Grande: K(q) function
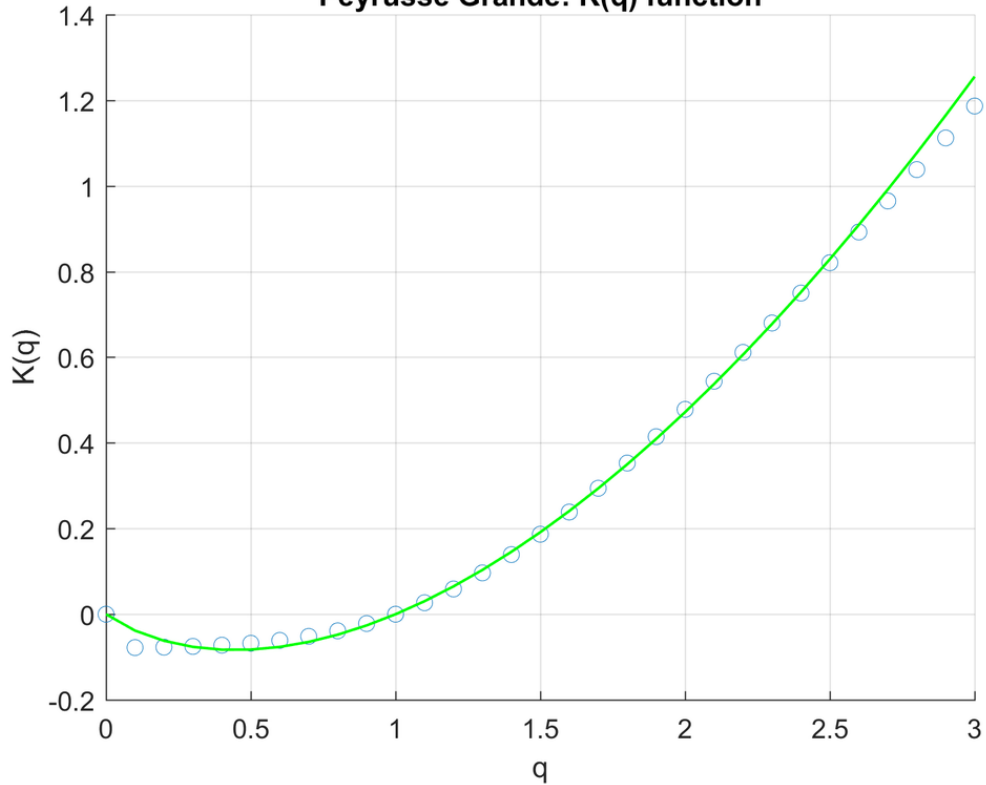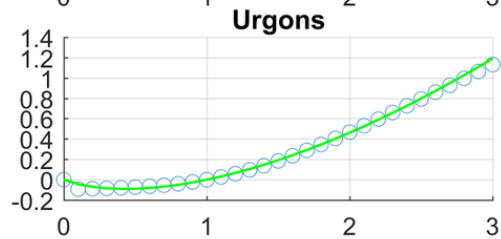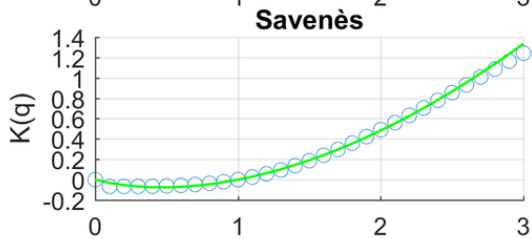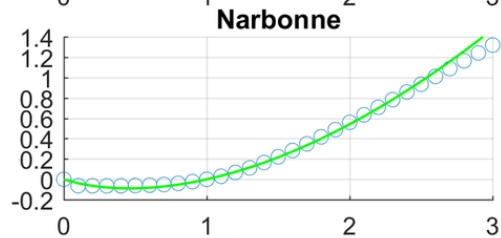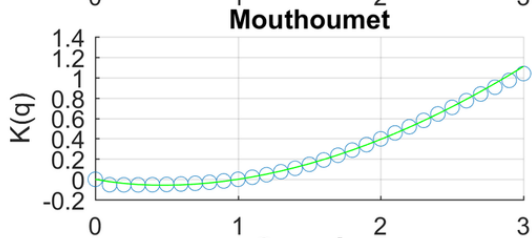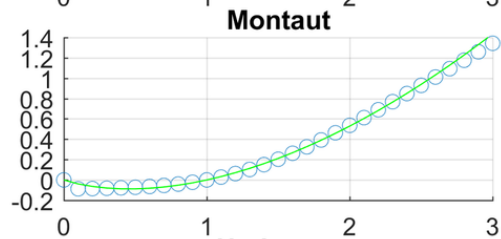
Condom · Créon d'Armagnac · Lahas · Montaut · Mouthoumet · Narbonne · Savenès · Urgons
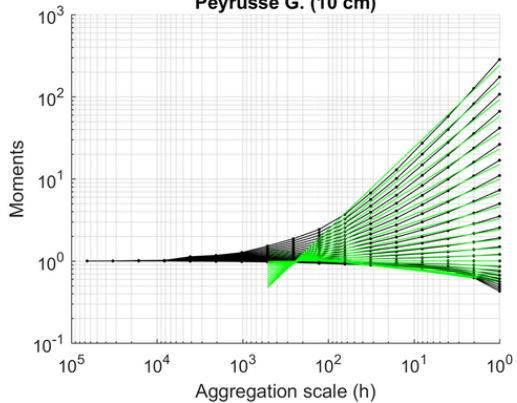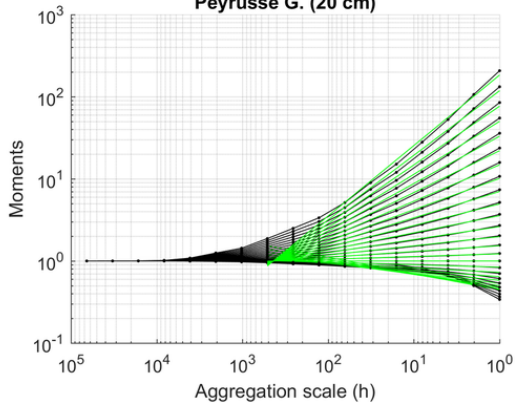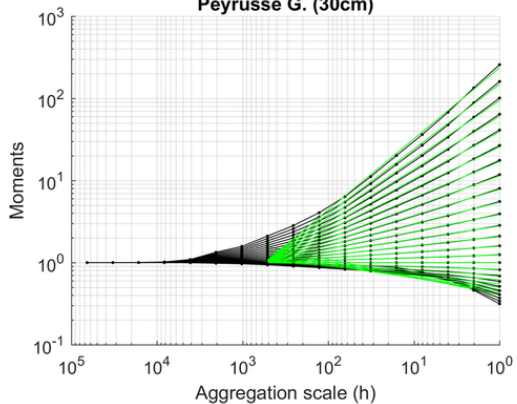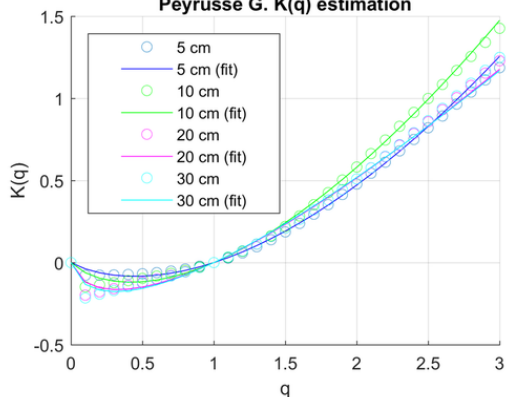
Parameter α for all time series
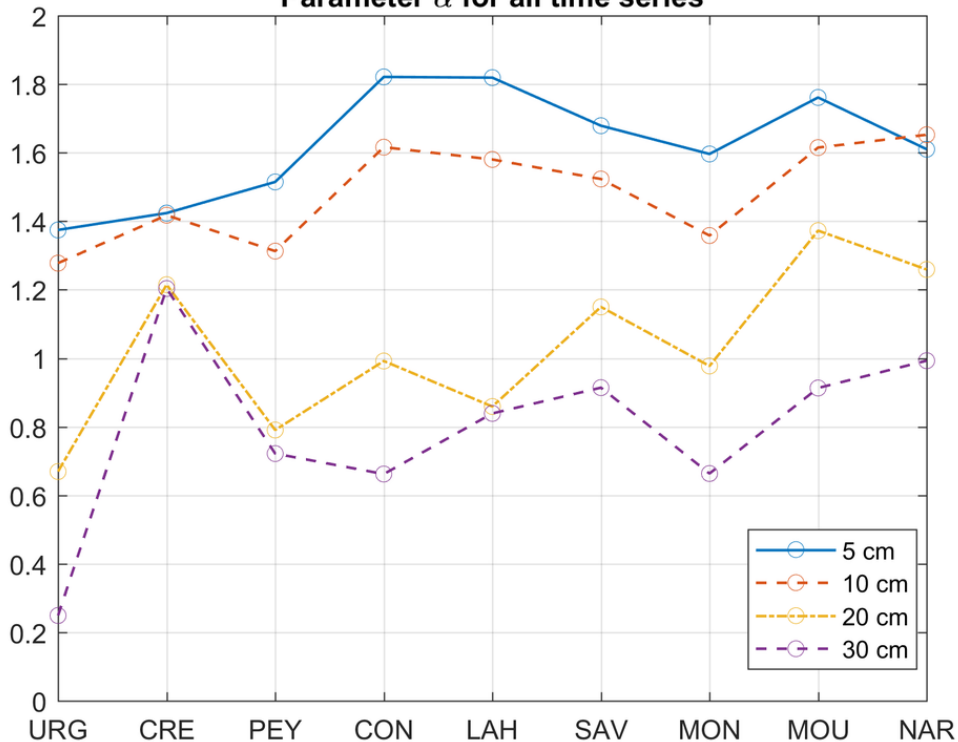
Parameter C_1 for all time series
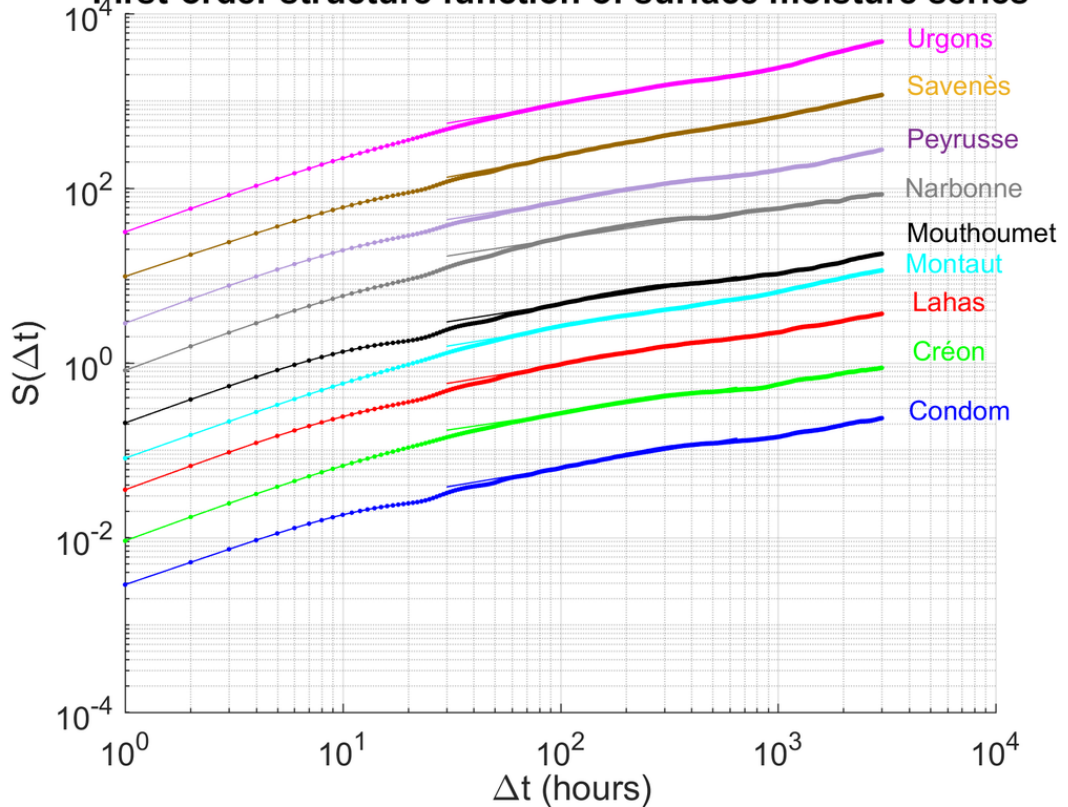
Legend:
- 5 cm
- 10 cm
- 20 cm
- 30 cm
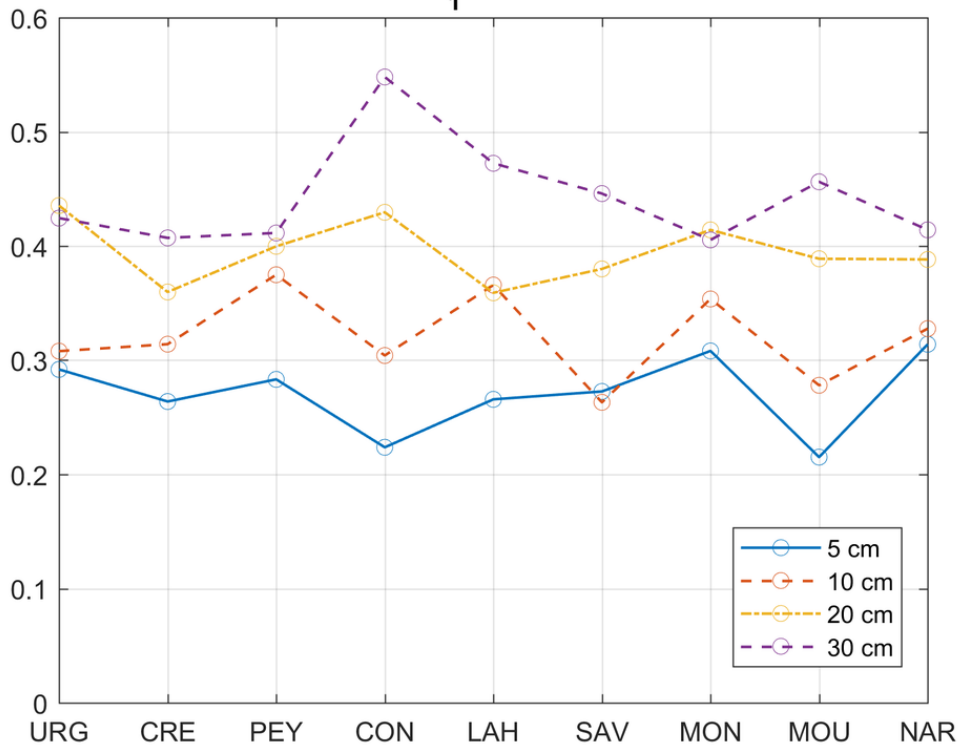
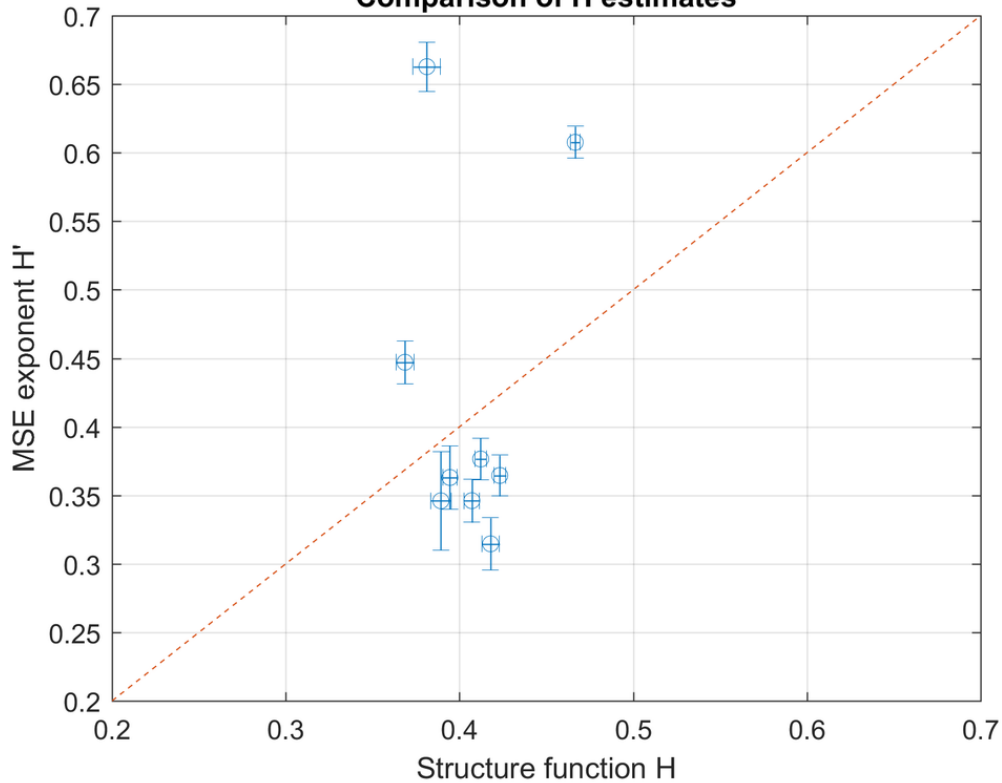**Multiscale Entropy of Soil Moisture series**
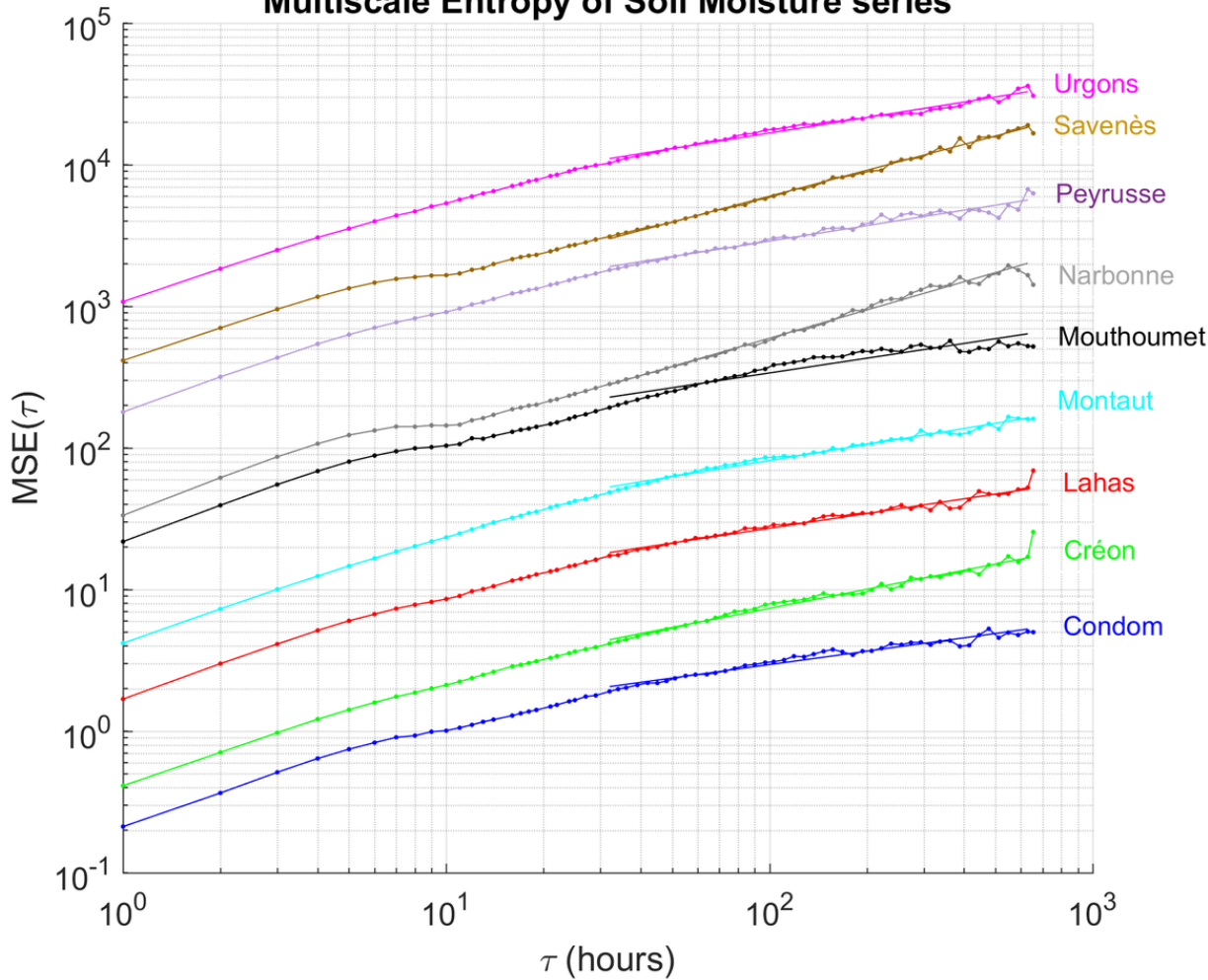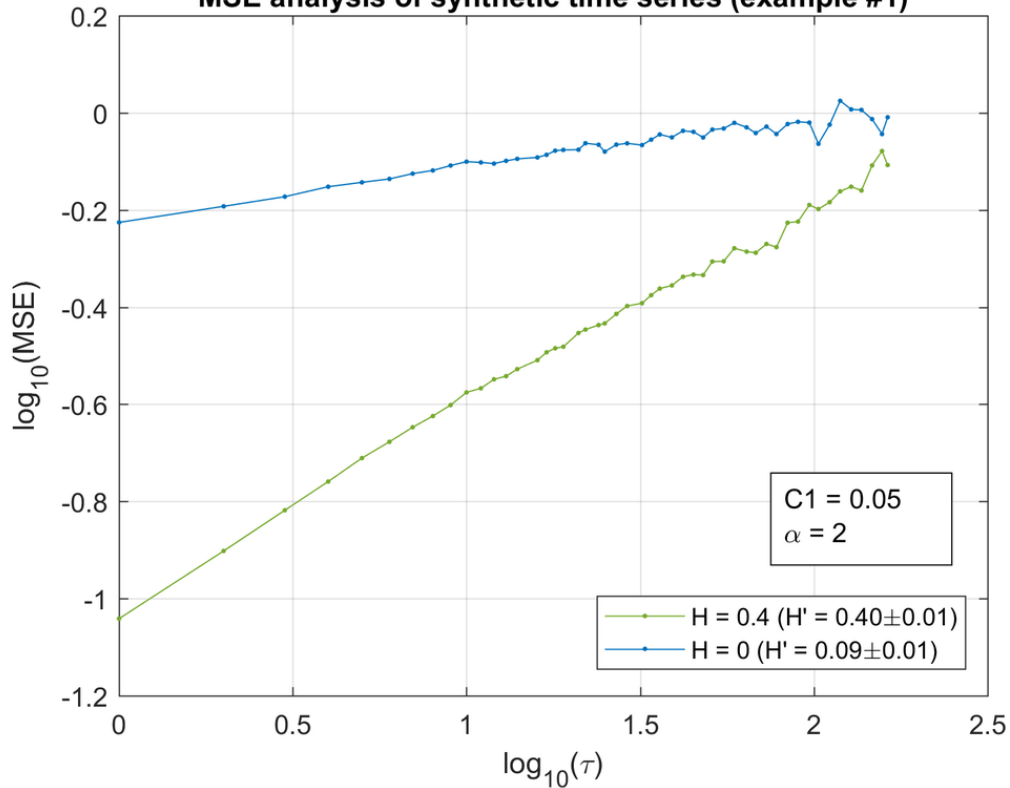
MSE scaling parameter H' for Smosmania time series
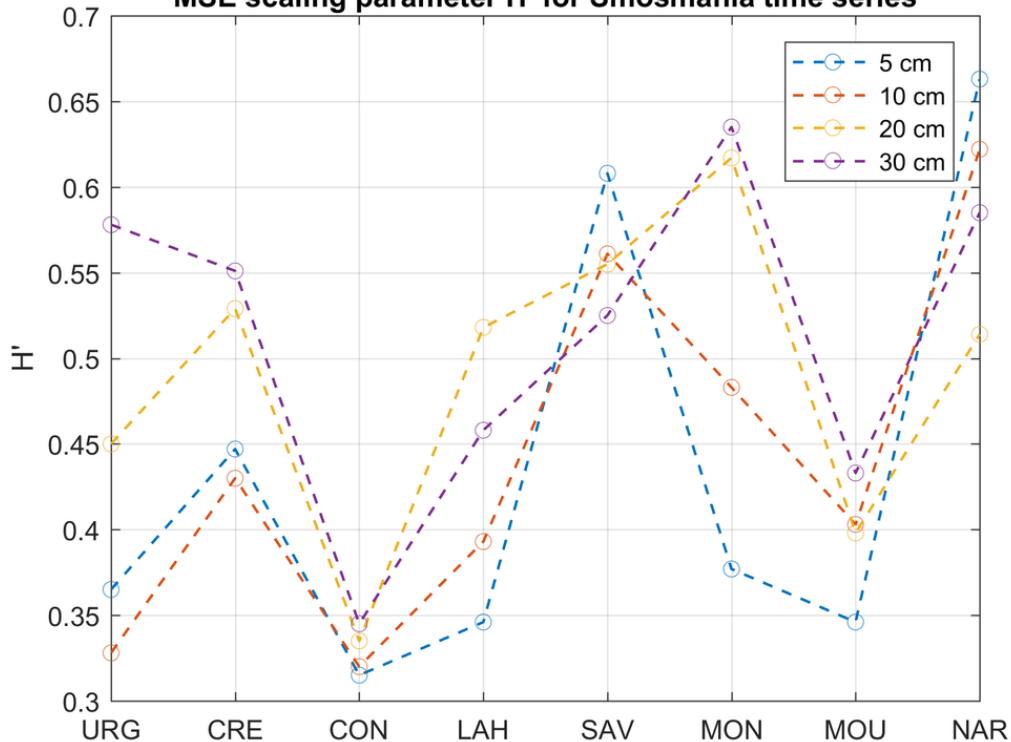
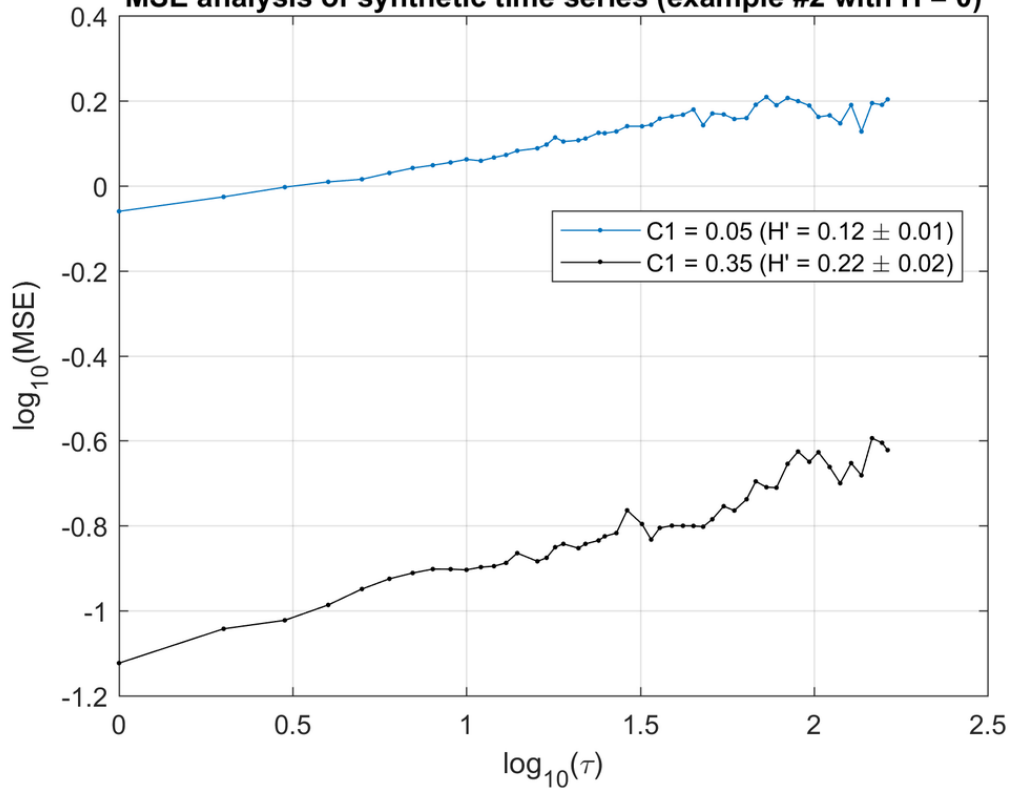First-order structure function of surface moisture series

Comparison of H estimates

MSE analysis of synthetic time series (example #1)

C1 = 0.05
α = 2

H = 0.4 (H' = 0.40±0.01)
H = 0 (H' = 0.09±0.01)

MSE analysis of synthetic time series (example #2 with H = 0)

Legend:
- C1 = 0.05 (H' = 0.12 ± 0.01)
- C1 = 0.35 (H' = 0.22 ± 0.02)

H' estimated from MSE analysis of synthetic time series

Legend:
- C1 = 0.05
- C1 = 0.15
- C1 = 0.25
- C1 = 0.35
- C1 = 0.45
- C1 = 0.55
- bisectrix

H' estimated from MSE analysis of synthetic time series